東京大学大学院新領域創成科学研究科
基盤科学研究系
先端エネルギー工学専攻

平成 17 年度

修士論文

Study on Propagation and Heating of Microwaves of Electron Cyclotron Range of Frequency on the Internal Coil Device Mini-RT

内部導体装置 Mini-RT での 電子サイクロトロン領域高周波の伝播・加熱特性

2006 年 2 月提出
指導教員　小川　雄一　教授

46213　谷塚　英一

Abstract

Electron cyclotron heating experiments were carried out on the internal coil device Mini-RT. As the background of this study, overdense plasma was generated on Mini-RT at the experiments with high temperature superconductor floating coil (F-Coil) levitated. Overdense means the electron (or ion) density exceeds cutoff density. Electromagnetic wave cannot propagate in such plasma. Thus it is necessary to investigate the mechanism of generation and heating of overdense plasma.

In this study consideration of possibility of heating by electron Bernstein wave were carried out. Conversion efficiency from electromagnetic wave to electron Bernstein wave depends on density, magnetic field strength and these characteristic gradient lengths. To change the density gradient length, we applied current to levitation coil (L-Coil) which is on the top of vacuum vessel and is normally used to levitate the F-Coil. Applying current leads to change plasma confinement region. In this study L-Coil were used for two objectives. One is the changing of plasma confinement region with F-Coil supported. And the other is levitating the F-Coil to avoid energy loss by support structure of F-Coil. We cannot achieve this two objectives simultaneously now (Feb.2006).

Measurements of electron density and electron temperature were carried out by using triple probe. Local maximum of electron temperature (LMET) appeared when applicable conditions were got. In this case the location of LMET almost coincides to the location of nth harmonic electron cyclotron resonance (ECR) on the extended line of electromagnetic wave injection.

These results give suggestions of possibility of mode conversion to electron Bernstein wave experimentally. In the case of cold plasma, absorption coefficient caused by 2nd, 3rd, $\cdots$ harmonics are extremely small since the electron Larmor radius is much smaller than wavelength of incident wave on Mini-RT while electron Bernstein wave has short wavelength comparable with electron Larmor radius at any harmonics of ECR.

Contents

List of Figures

List of Tables

Chapter 1

Introduction

1.1 Study on high beta plasma

To study high beta plasma is interesting. Beta is defined as follows.

$$\beta = \frac{\sum_{j=i,e} n_j \kappa T_j}{\frac{B^2}{2\mu_0}} \tag{1.1}$$

Here, κ is the Boltzmann constant.

High beta means that plasma is confined in relatively weak magnetic field. As well known, we must generate high density and high temperature plasma and confine it in order to satisfy the Lawson criterion. Thus beta is an important parameter in the magnetic confinement fusion research.

Although particle confinement time is long in strong magnetic field, it is inefficient to confine plasma with strong magnetic field. Because large coil and its support structure will be needed to create strong magnetic field. Such reactor is not economical. Furthermore radiation from plasma increases with the strength of magnetic field.

Recently high beta plasma studies are carrying out on various devices, e.g., Spherical Torus (ST) and Field Reversed Configuration (FRC). For example, heating without Ohmic heating (Center Solenoid Coil) is studied to establish low aspect ratio plasma on ST devices [1].

With only Radio frequency (RF) heating, since the cutoff density exists, it is hard to generate and heat high density plasma. For example, cutoff density is $7.4 \times 10^{16} m^{-3}$ for 2.45GHz Ordinary Mode (O-Mode) injection. Cutoff density is determined by frequency of incident electromagnetic wave, and cyclotron frequency is determined by magnetic field

strength. In order to generate high beta plasma with only RF heating, some scheme to generate and heat overdense plasma, i.e., $\omega_{pe} > \Omega_e$, is required. Here, ω_{pe} and Ω_e are the electron plasma frequency and the electron cyclotron frequency respectively.

Mode conversion from electromagnetic wave (EMW) to Electron Bernstein wave (EBW) is valuable method to heat overdense plasma. There is no cutoff density for EBW [2]. Recently, on many devices, e.g. National Spherical Torus eXperiment (NSTX) [3] and W7-AS Stellarator [4], study of conversion to EBW was carried out.

On Mini-RT, generation of overdense plasma was achieved however the mechanism of generation and heating of overdense plasma did not become clear.

1.2 Study on Internal Coil Device

In this section, study with internal coil device is reviewed.

Magnetic well and magnetic shear effects were shown by experiments on internal coil devices . Representative example of those devices are Octapole [5], Levitron[6], Spherator[7]. Especially, levitated version Spherator achieved several hundreds times longer particle confinement time than Bohm time, i.e., $\tau_p >\sim 300\tau_B$ [8]. However, many of internal coil devices were shut down due to difficulty in the application to fusion reactors in the 1970s.

Recently, study on internal coil device from the new point of view were launched. Planetary explorer satellite Voyager 2 found extremely high beta plasma in the Jupiter's magnetosphere [9]. A. Hasegawa discussed about interchange instability and discovered high beta equilibrium state in dipole magnetic configuration [10]. MIT and Columbia University constructed an internal coil device called LDX (Levitated Dipole eXperiment) based on Hasegawa's theory.

S.M. Mahajan and Z. Yoshida predicted high beta equilibrium state based on relaxation theory [11] [12]. They considered not only electron's flow (electric current) but also ion's flow (plasma flow) and solved variational problem under the constraint of magnetic helicity and generalized helicity. Based on their theory, an internal coil device called RT-1 (Ring Trap 1) was constructing at University of Tokyo (Jan. 2006).

Study on Mini-RT is based on Mahajan and Yoshida's theory. Details of Mini-RT are explained at chapter 2.

1.3 Objective of this Study

The objective of this study is to achieve generation of overdense plasma and to understand the mechanism of heating overdense plasma under the relatively simple magnetic field on torus device. On Mini-RT device, plasma is heated by electron cyclotron heating (ECH) (2.45GHz, 2.8kW c.w.). In this study Electron Bernstein Wave heating is regarded as the mechanism of generation and heating of overdense plasma.

To demonstrate the possibility of EBW heating, following procedure was employed. Propagation and absorption of EBW which does not have cutoff density is discussed by considering the dispersion relation of EBW from measured electron density and temperature profile.

1.4 Constitution of this Paper

Chapter 2 explains about internal coil device Mini-RT. Chapter 3 shows the review of physics on radio-frequency waves of electron cyclotron range of frequency. Chapter 4 describes the experimental set up. Chapter 5 gives the results. Chapter 6 discusses about future plans. Finally, chapter 7 gives summary.

Chapter 2

Internal Coil Device Mini-RT

In this chapter, the review of the internal coil device Mini-RT is shown.

2.1 Mechanical Structure

Figure 2.1 shows the cross section of Mini-RT. Toroidal Coils, Vertical Coils and Saddle Coils do not exist now(Feb.2006).

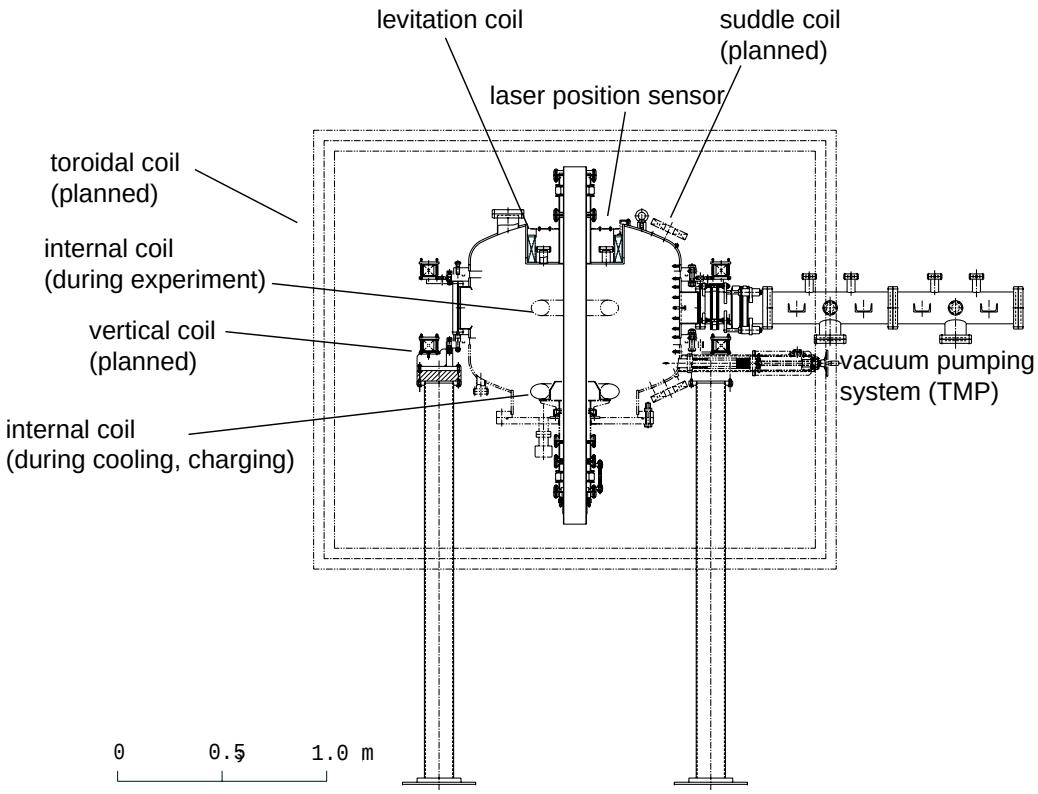

Figure 2.1: Cross Section of Mini-RT

The specifications of vacuum vessel and coils are shown in Table 2.1 and 2.2 respectively.

Table 2.1: Specification of vacuum vessel of Mini-RT

Diameter	1.0m
Height	0.7m
Base Pressure	1.0×10^{-5}Pa

Table 2.2: Specification of coils

Internal Coil (F-Coil)	
Material	Bi-2223 tape
Major Radius	150mm
Outer Radius of Coil Shell	210mm
Inner Radius of Coil Shell	122mm
Turn Number	428
Total Current	50kA
Total Weight	16.8kg
Inductance	0.0876H
Stored Energy	598J
Levitation Coil (L-Coil)	
Material	Copper(water-cooled)
Major Radius	208.75mm
Turn Number	68
Total Current	27kA

Internal Coil (F-Coil) is cooled to 20K at the bottom of vacuum vessel by helium gas through the detachable transfer tube. F-Coil is charged by direct excitation with persistent current switch (PCS) [13] [14]. The current feedthrough is also detachable. Temperature of F-Coil and PCS are measured by temperature sensor PtCo and Cernox, respectively.

F-Coil is supported by support structure. Figure 2.2 shows the photograph of plasma with supported F-Coil.

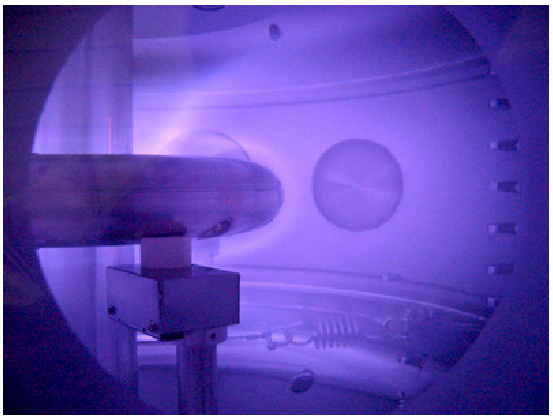

Figure 2.2: Photograph of Plasma with Supported F-Coil

2.2 Magnetic Configuration

Two types of magnetic configuration can be composed. One is the simple dipole configuration drawn in Fig.2.3. Another is called regular configuration drawn in Fig.2.4. Each configurations are constructed only poloidal magnetic field, thus no magnetic shear by extra magnetic field exists.

Figure 2.3 shows the magnetic configuration when magnetic field is composed only F-Coil (I_F=50kA, I_L=0A). Since L-Coil is not charged, experiments with F-coil supported is only possible. Plasma is limited by vacuum vessel wall.

Fig.2.4 shows the magnetic configuration when magnetic field is composed F-Coil and L-Coil (I_F=50kA, I_L=15kA). If the L-Coil current is sufficiently large to levitate the F-Coil, experiments are carried out with F-Coil levitated. If the L-Coil current is not so large, experiments are carried out with F-Coil supported. Plasma is limited by separatorix.

Dipole magnetic field has steep gradient. The relationship between magnetic field strength B and major radius on the equatorial plane r is approximately $B \propto r^{-3}$ for sufficiently large r. On the other hand, in many devices like tokamak, $B_t \propto r^{-1}$ is implemented, here subscript t means toroidal direction. The steep gradient of magnetic field plays important role of conversion from electromagnetic wave to EBW.

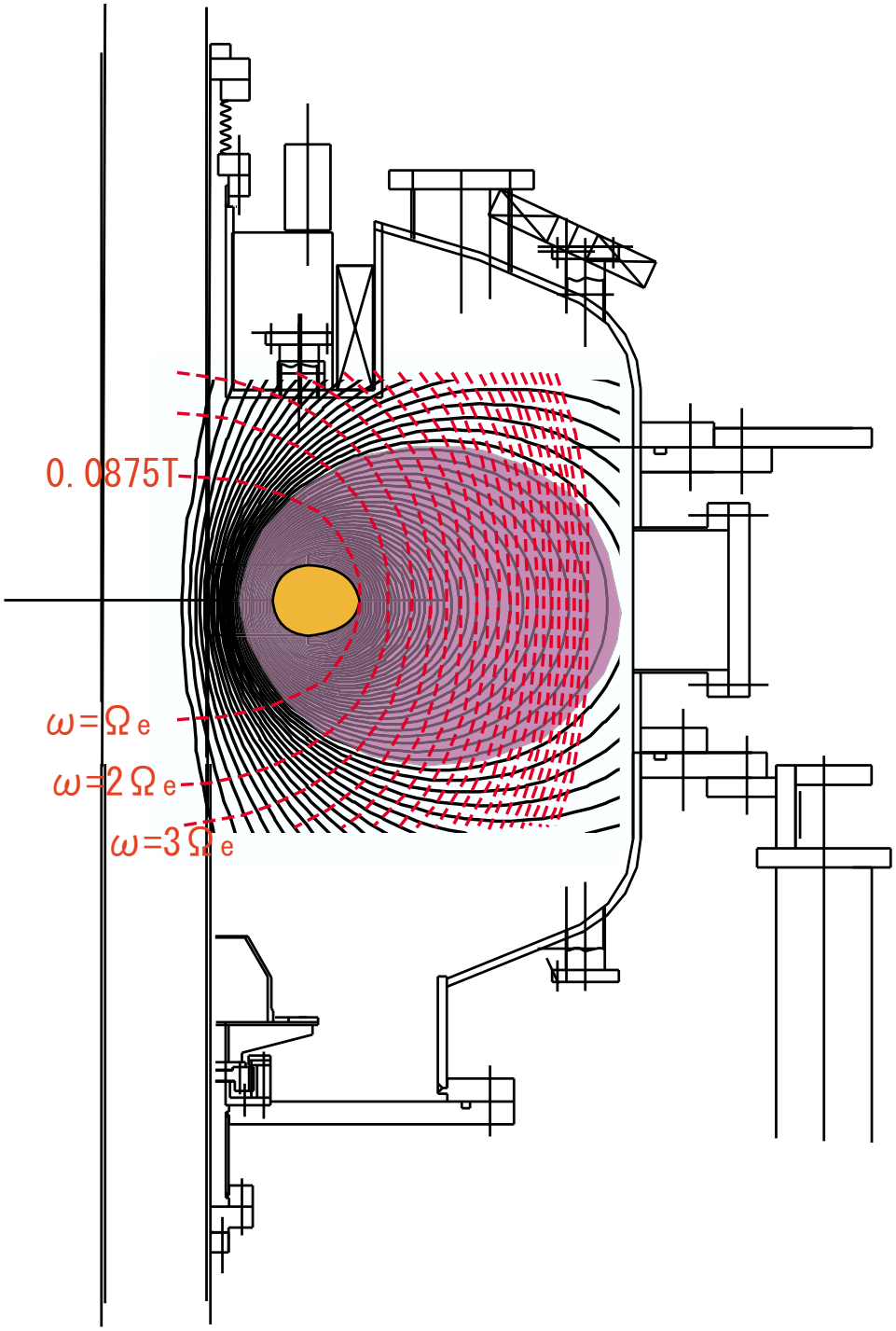

Figure 2.3: Dipole Configuration; Solid lines and dotted lines show the magnetic flux surface and contour of magnetic field strength respectively. Contour represents nth harmonic ECR (n=1,2,...,20).

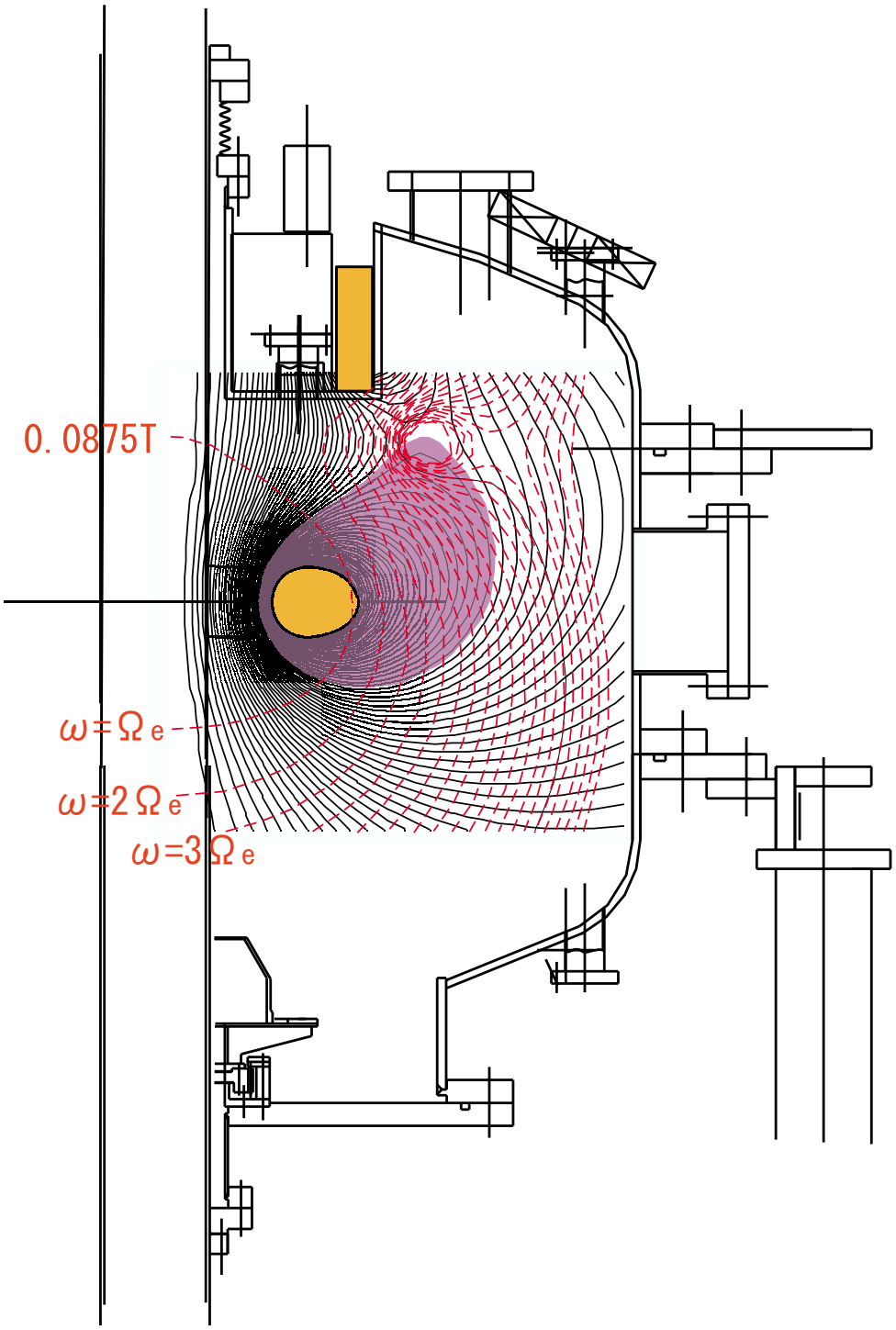

Figure 2.4: Regular Configuration; Solid lines and dotted lines have the same meaning of Fig.2.3. Plasma confinement region is determined by separatorix which appears between L-Coil and F-Coil. And location of separatorix is determined by the ratio of F-Coil current and L-Coil one.

2.3 Levitation Control

In Mini-RT, pull-up method was adopted for position control of F-Coil. As shown in Fig.2.5, rigid body has 6 degrees of freedom, i.e. 3 translational directions and 3 rotational directions. There is not necessity for plasma experiments to control the rotational motion around z axis. Table 2.3 shows the stability of levitation with regular configuration of Mini-RT [15]. Feedback control for unstable direction is needed.

Table 2.3: Levitation Stability of Mini-RT

Vertical	Unstable
Sliding	Stable
Tilting	Stable

The motion along z direction is controlled by PID control of the L-Coil current[16]. The vertical position z of F-Coil is detected by three laser position sensors (Keyence LK-500 (sensor head), LK-2500 (amplifier unit)). The accuracy of levitation control is 50μm (long mode). Fig.2.6 shows a photograph of plasma with levitated F-Coil.

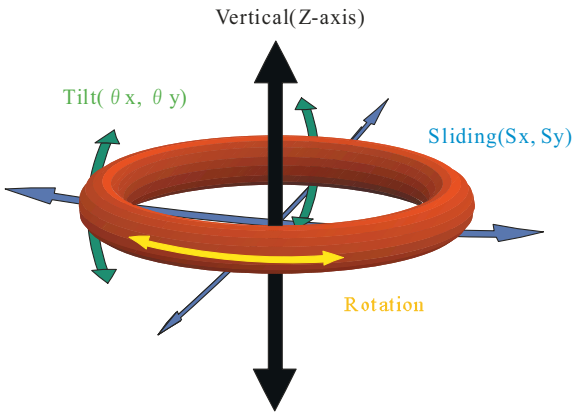

Figure 2.5: Degrees of Freedom of F-Coil

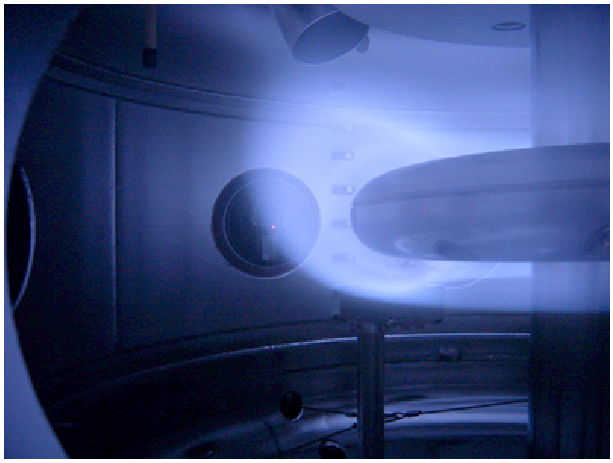

Figure 2.6: Photograph of Plasma with Levitated F-Coil

2.4 Plasma Heating

Plasma is generated by Electron Cyclotron Heating (ECH) on Mini-RT. Table 2.4 shows the frequency and power of ECH.

Table 2.4: ECH System of Mini-RT

Frequency	2.45GHz
Power	2.8kW C.W.
Output Ripple	$10\%_{\mathrm{p-p}}$
Incident Angle to Vertical	30°

ECH injection mode is determined by the waveguide. Figure 2.7 is a photograph of Mini-RT and its ECH system. Figures 2.8 and 2.9 are photographs of waveguides for O-Mode and X-Mode injection respectively.

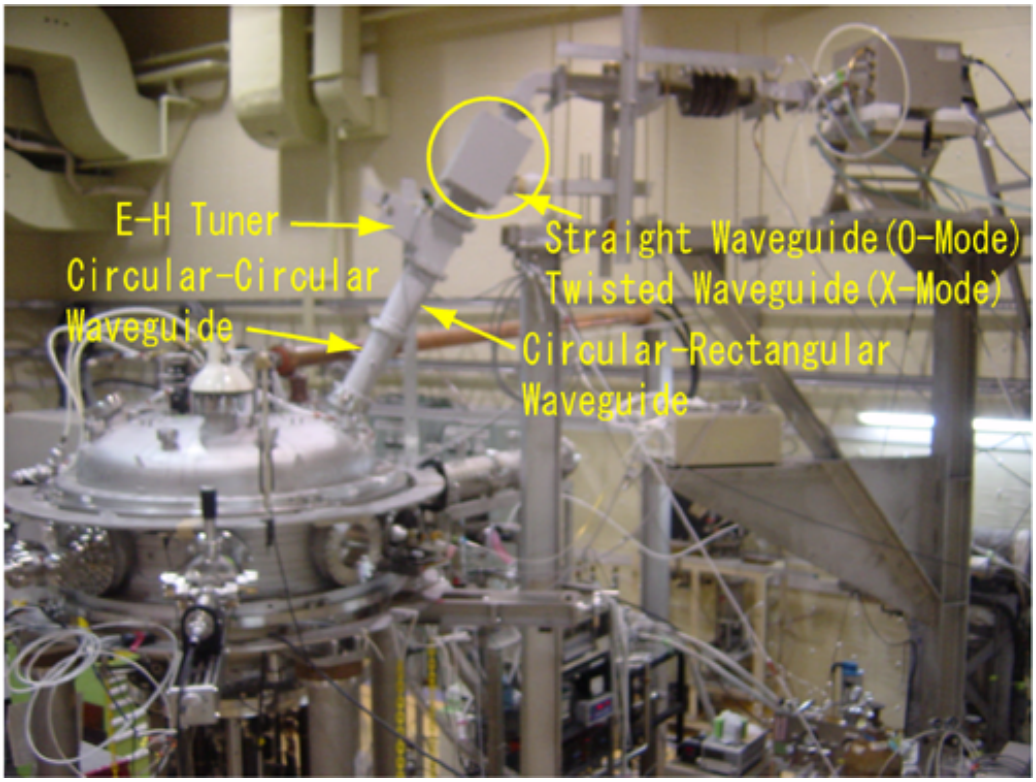

Figure 2.7: ECH system of Mini-RT

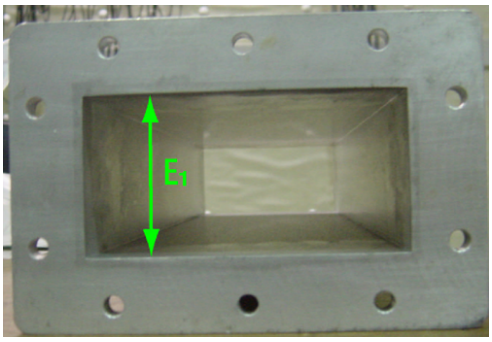

Figure 2.8: Waveguide for O-Mode Injection

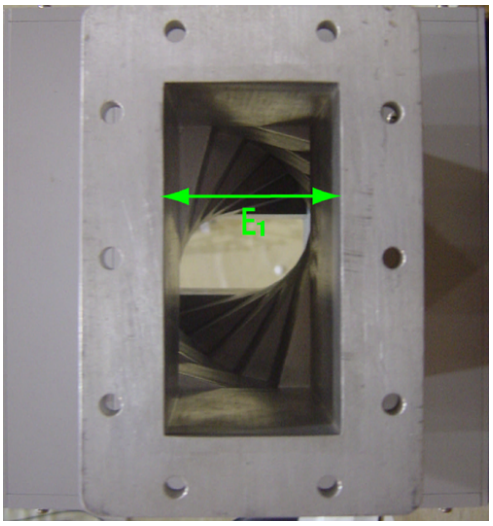

Figure 2.9: Waveguide for X-Mode Injection

Electric field in waveguides is directed to the direction of narrow side of waveguide. Magnetic field generated by F-Coil is directed poloidal direction. If straight waveguide is used, electric field is directed poloidal direction (O-Mode injection). To the contrary, twisted waveguide is used for X-Mode injection, i.e. electric field is directed to toroidal direction.

Chapter 3

Study on Radiofrequency Waves of Electron Cyclotron Range of Frequency on Mini-RT

In this chapter, propagation and absorption of radiofrequency wave on Mini-RT are reviewed. First, the review of cold plasma wave is shown. Second, hot plasma wave is mentioned. Third, outline of mode conversion to EBW is presented. Finally, absorption of the energy of wave is reviewed.

Radiofrequency wave in plasma is often analyzed by using cold plasma wave approximation. This approximation is well effected when the wavelength is much longer than Larmor radius. If the wavelength is shorter than or comparable with electron Larmor radius, i.e. the refractive index is sufficiently large (resonance), cold plasma wave approximation falls.

EBW is electrostatic wave excited on hot plasma and it propagates perpendicular to magnetic field. The wavelength of EBW is comparable with electron Larmor radius. EBW does not have cutoff density and resonate at the harmonics of electron cyclotron resonance frequency.

At the last of this chapter absorption of electromagnetic wave and EBW is mentioned. Power absorption per unit volume is derived by using the dielectric tensors which are derived in this chapter. Derived absorption coefficients of harmonic cyclotron damping are used for consideration of experimental results.

3.1 Cold Waves

3.1.1 Dispersion Relation

Dispersion relation of cold plasma wave is determined by Maxwell equation.

$$\nabla \cdot \mathbf{E} = \frac{\rho}{\epsilon_0} \tag{3.1}$$

$$\nabla \cdot \mathbf{B} = 0 \tag{3.2}$$

$$\nabla \times \mathbf{E} = -\frac{\partial \mathbf{B}}{\partial t} \tag{3.3}$$

$$\nabla \times \mathbf{B} = \frac{1}{c^2}\frac{\partial \mathbf{E}}{\partial t} + \mu_0 \mathbf{j} \tag{3.4}$$

Here ρ and $\mathbf{j}$ denote charge density and current density respectively, which are determined by 0th and 1st moment of distribution function.

$$\rho = \sum_j q_j \int d^3v f_j \tag{3.5}$$

$$\mathbf{j} = \sum_j q_j \int d^3v f_j \mathbf{v} \tag{3.6}$$

Then f_j and q_j denote the distribution function and charge of "j" respectively and j denotes specie.

The time development of distribution function follows Vlasov equation.

$$\frac{\partial f_j}{\partial t} + \mathbf{v} \cdot \nabla_r f_j + \frac{q_j}{m_j}(\mathbf{E} + \mathbf{v} \times \mathbf{B}) \cdot \nabla_v f_j = 0 \tag{3.7}$$

Here m denotes mass. Use the notation $f_j = f_{j0} + f_{j1}$, $\mathbf{B} = \mathbf{B_0} + \mathbf{B_1}$, $\mathbf{E} = \mathbf{E_1}$. Then suffix 0 denotes the value without perturbation and suffix 1 denotes the value with perturbation.

Assume plasma is cold, i.e. $T_j = 0$. Zeroth order of distribution function f_{j0} is written as

$$f_{j0} = n_{j0}\delta(\mathbf{v}) = n_{j0}\delta(v_x)\delta(v_y)\delta(v_z). \tag{3.8}$$

Take the 1st moment of $\mathbf{v}$ of (3.7), and equation of motion of magnetofluid is led.

$$n_j m_j \frac{d\mathbf{u}_j}{dt} = n_j q_j(\mathbf{E} + \mathbf{u} \times \mathbf{B}) - \nabla \cdot \Phi_j, \tag{3.9}$$

$$\frac{d}{dt} = \frac{\partial}{\partial t} + \mathbf{v} \cdot \nabla \tag{3.10}$$

Here $\mathbf{u}_j$ denotes the mean velocity of j.

$$\mathbf{u}_j = \int d^3v f_j v = \frac{\mathbf{j}_j}{q_j n_j} \tag{3.11}$$

And Φ_j is pressure tensor of j. Since no broadening of distribution function exists, Φ_j goes to zero. Thus Eq.(3.9) is written like a equation of motion of single particle.

$$m_j \frac{d\mathbf{u}_j}{dt} = q_j(\mathbf{E} + \mathbf{u} \times \mathbf{B}) \tag{3.12}$$

Equations (3.11) and (3.12) gives relationship between current density and electric field, i.e. dielectric tensor is given from these equations. Neglect the convective term of Eq.(3.12) and assume the perturbed fields vary as $\exp[i(\mathbf{k} \cdot \mathbf{x} - \omega t)]$.From the Eq.(3.4) electric displacement $\mathbf{D}$ is defined as follows

$$\mathbf{D}(\omega, \mathbf{k}) = \epsilon_0 \mathbf{E}(\omega, \mathbf{k}) + \frac{i}{\omega}\mathbf{j}(\omega, \mathbf{k}) \equiv \overleftrightarrow{\epsilon}(\omega, \mathbf{k}) \cdot \mathbf{E}(\omega, \mathbf{k}) \tag{3.13}$$

$$\mathbf{j} = \sum_j \mathbf{j}_j = \sum_j \overleftrightarrow{\sigma_j} \cdot \mathbf{E} = \sum_j (-i\omega\epsilon_0)\overleftrightarrow{\chi_j} \cdot \mathbf{E} \tag{3.14}$$

$$\overleftrightarrow{\epsilon} = \epsilon_0(\overleftrightarrow{I} + \sum_j \overleftrightarrow{\chi}_j) \tag{3.15}$$

where $\overleftrightarrow{\epsilon}$, $\overleftrightarrow{\sigma}$, $\overleftrightarrow{\chi}$ and $\overleftrightarrow{I}$ are the dielectric tensor, the conductivity tensor, the susceptibility tensor and the unit tensor.

Dielectric tensor of cold plasma is written as

$$\overleftrightarrow{\epsilon} \cdot \mathbf{E} = \epsilon_0 \begin{pmatrix} S & -iD & 0 \\ iD & S & 0 \\ 0 & 0 & P \end{pmatrix} \tag{3.16}$$

where $\mathbf{B}_0 = B_0\hat{z}$ is assumed and

$$S = \frac{1}{2}(R + L) \tag{3.17}$$

$$D = \frac{1}{2}(R - L) \tag{3.18}$$

$$R \equiv 1 + \sum_j \chi_j^- = 1 - \sum_j \frac{\omega_{pj}^2}{\omega(\omega + \Omega_j)} \tag{3.19}$$

$$L \equiv 1 + \sum_j \chi_j^+ = 1 - \sum_j \frac{\omega_{pj}^2}{\omega(\omega - \Omega_j)} \tag{3.20}$$

$$\chi_j^{\pm} \equiv \frac{1}{2}(\chi_x \pm i\chi_y) \tag{3.21}$$

where ω_p and Ω are plasma frequency and cyclotron frequency respectively.

$$\omega_{pj}^2 = \frac{n_j q_j^2}{\epsilon_0 m_j} \tag{3.22}$$

$$\Omega_j = \frac{q_j B_0}{m_j} \tag{3.23}$$

Coupling Eqs.(3.3) with (3.4), wave equation is obtained.

$$\mathbf{k} \times \mathbf{k} \times \mathbf{E} + \frac{\omega^2}{c^2} \left(\overleftrightarrow{I} + \sum_j \overleftrightarrow{\chi}_j \right) \cdot \mathbf{E} = 0 \tag{3.24}$$

Refractive index vector $\mathbf{n}$ is defined as

$$\mathbf{n} \equiv \frac{\mathbf{k}c}{\omega}, \tag{3.25}$$

Eq.(3.24) is written as

$$\mathbf{n} \times \mathbf{n} \times \mathbf{E} + \left(\overleftrightarrow{I} + \sum_j \overleftrightarrow{\chi}_j \right) \cdot \mathbf{E} = 0. \tag{3.26}$$

If we assume $\mathbf{n}$ is on the x-z plane and we use θ to denote the angle formed by the meeting of $\mathbf{B}_0$ with $\mathbf{n}$, i.e. $\cos\theta = \hat{z} \cdot \mathbf{n}$, Eq.(3.26) becomes

$$\begin{pmatrix} S - n^2\cos^2\theta & -iD & n^2\cos\theta\sin\theta \\ iD & S - n^2 & 0 \\ n^2\cos\theta\sin\theta & 0 & P - n^2\sin^2\theta \end{pmatrix} \begin{pmatrix} E_x \\ E_y \\ E_z \end{pmatrix} \equiv \mathbf{\Lambda}_c \cdot \mathbf{E} = 0. \tag{3.27}$$

Dispersion relation of cold plasma wave is

$$\det \mathbf{\Lambda}_c = 0. \tag{3.28}$$

Then Eq.(3.27) has nontrivial solutions of $\mathbf{E}$ [17]. Eq.(3.28) is a biquadratic equation.

$$An^4 - Bn^2 + C = 0 \tag{3.29}$$

$$A \equiv S\sin^2\theta + P\cos^2\theta \tag{3.30}$$

$$B \equiv RL\sin^2\theta + PS(1 + \cos^2\theta) \tag{3.31}$$

$$C \equiv PRL \tag{3.32}$$

There are two solutions of Eq.(3.29) involving imaginary number.

$$n^2 = \frac{B \pm F}{2A} \tag{3.33}$$

$$F^2 \equiv (RL - PS)^2 \sin^4\theta + 4P^2D^2\cos^2\theta \tag{3.34}$$

Especially, consider the perpendicular injection.

$$n^2 = \begin{cases} P & \text{(O-Mode)} \\ \dfrac{RL}{S} & \text{(X-Mode)} \end{cases} \tag{3.35}$$

3.1.2 Cutoff, Resonance and Absorption

Cutoff occurs when the refractive index goes to zero. The necessary condition of cutoff is

$$PRL = 0. \tag{3.36}$$

Especially, consider the perpendicular injection.

$$\begin{aligned} P = 0 \quad & \text{(O-Mode)} \\ R = 0, L = 0 \quad & \text{(X-Mode)} \end{aligned} \tag{3.37}$$

In contrast, resonance occurs when the refractive index goes to infinity. The necessary condition of it is

$$\tan^2\theta = -\frac{P}{S}. \tag{3.38}$$

Correspondingly, consider the perpendicular injection.

$$S = 0 \quad \text{(X-Mode)} \tag{3.39}$$

There are two solutions of (3.39), one is called Upper Hybrid Resonance (UHR) and the other is called Lower Hybrid Resonance (LHR).

$$\omega^2 = \omega_{pe}^2 + \Omega_e^2 \quad \text{(UHR)} \tag{3.40}$$

$$\frac{1}{\omega^2} = \frac{1}{\Omega_i^2 + \omega_{pi}^2} + \frac{1}{\Omega_i|\Omega_e|} \quad \text{(LHR)} \tag{3.41}$$

Energy absorption of wave occurs at resonance. Details of absorption condition is shown in latter section.

3.2 Hot Waves

3.2.1 Dispersion Relation of hot wave for arbitrary f_0

The principle of solving the dispersion relation of hot plasma is almost identical to that of cold plasma. The difference is how to solve Vlasov equation (Eq.(3.7)). Larmor motion must be considered and interesting phenomena, e.g. harmonic resonance, is derived.

Linearize Eqs.(3.1)-(3.4) and (3.7). Nontrivial 0th order equations are

$$\mathbf{v} \cdot \nabla_r f_{j0} + \frac{q_j}{m_j} (\mathbf{v} \times \mathbf{B}_0) \cdot \nabla_v f_{j0} = 0 \tag{3.42}$$

$$\sum_j q_j \int d^3v f_{j0} = 0 \tag{3.43}$$

$$\frac{1}{\mu_0} \nabla \times \mathbf{B}_0 = \sum_j q_j \int d^3v \mathbf{v} f_{j0} = \mathbf{j}_0 \tag{3.44}$$

and 1st order equations are

$$\frac{df_j}{dt} = \frac{\partial f_{j1}}{\partial t} + \mathbf{v} \cdot \nabla_r f_{j1} + \frac{q_j}{m_j} (\mathbf{v} \times \mathbf{B}_0) \cdot \nabla_v f_{j1} = -\frac{q_j}{m_j} (\mathbf{E}_1 + \mathbf{v} \times \mathbf{B}_1) \cdot \nabla_v f_{j0} \tag{3.45}$$

$$i\mathbf{k} \cdot \mathbf{E}_1 = \frac{1}{\epsilon_0} \sum_j q_j \int d^3v f_{j1} \tag{3.46}$$

$$\frac{1}{\mu_0} \mathbf{k} \times \mathbf{B}_1 = -\omega(\epsilon_0 \mathbf{E}_1 + \frac{i}{\omega} \sum_j q_j \int d^3v \mathbf{v} f_{j1}) \tag{3.47}$$

$$\mathbf{B}_1 = \frac{1}{\omega} (\mathbf{k} \times \mathbf{E}_1). \tag{3.48}$$

Distribution function without perturbation f_{j0} must meet Eqs.(3.42)-(3.44). Equation (3.45) formulates that perturbed distribution function f_{j1} is determined by superimposed perturbation field ($\mathbf{E}_1$ and $\mathbf{B}_1$) of f_{j0}.

Integrate Eq.(3.45) with respect to time along the trajectory of particle in phase space.

$$f_{j1}(\mathbf{r}, \mathbf{v}, t) = -\frac{q_j}{m_j} \int_{-\infty}^{t} [\mathbf{E}_1(\mathbf{r}'(t'), t') + \frac{1}{\omega} \mathbf{v}'(t') \times (\mathbf{k} \times \mathbf{E}_1(\mathbf{r}'(t'), t'))] \cdot \nabla'_v f_{j0}(\mathbf{r}'(t'), t') dt' \tag{3.49}$$

Then $\mathbf{r}'$ is the 0th order of orbit (Larmor orbit). Considering $\mathbf{r}'(t) = \mathbf{r}$ and $\mathbf{v}'(t) = \mathbf{v}$, we can obtain Larmor orbit.

$$v'_x(t') = v_\perp \cos[\theta - \Omega(t' - t)] \tag{3.50}$$

$$v'_y(t') = v_\perp \sin[\theta - \Omega(t' - t)] \tag{3.51}$$

$$v_z'(t') = v_z \tag{3.52}$$

$$x'(t') = x - \frac{v_\perp}{\Omega}(\sin[\theta - \Omega(t'-t)] - \sin\theta) \tag{3.53}$$

$$y'(t') = y + \frac{v_\perp}{\Omega}(\cos[\theta - \Omega(t'-t)] - \cos\theta) \tag{3.54}$$

$$z'(t') = z + v_z(t'-t) \tag{3.55}$$

Substituting Eqs.(3.50)-(3.55) into Eq.(3.49) and using formulae of Bessel function,

$$\exp(ia\sin\theta) = \sum_{m=-\infty}^{\infty} J_m(a)\exp(im\theta) \tag{3.56}$$

$$J_{-m}(a) = (-1)^m J_m(a) \tag{3.57}$$

we can obtain f_{j1}.

$$f_{j1}(\mathbf{r},\mathbf{v},t) = -\frac{q_j}{m_j}e^{i(k_x x + k_z z - \omega t)}\sum_{m,n}\Big[U_j\left(\frac{J_{n-1}+J_{n+1}}{2}\right)E_x$$
$$-iU_j\left(\frac{J_{n-1}-J_{n+1}}{2}\right)E_y + \left(W_j\frac{J_{n-1}+J_{n+1}}{2} + \frac{\partial f_{j0}}{\partial v_z}\right)E_z\Big]\frac{J_m\exp(i(m-n)\theta)}{i(k_z v_z - \omega - n\Omega)} \tag{3.58}$$

Here

$$U_j = \left(1 - \frac{k_z v_z}{\omega}\right)\frac{\partial f_{j0}}{\partial v_\perp} + \frac{k_z v_\perp}{\omega}\frac{\partial f_{j0}}{\partial v_z} \tag{3.59}$$

$$W_j = \frac{k_x v_z}{\omega}\frac{\partial f_{j0}}{\partial v_\perp} - \frac{k_x v_\perp}{\omega}\frac{\partial f_{j0}}{\partial v_z} \tag{3.60}$$

and $J_n = J_n(a_j)$ is the nth Bessel function which has the argument a_j.

$$a_j = \frac{k_x v_\perp}{\Omega_j} = k_x \rho_j \tag{3.61}$$

Here ρ_j is the Larmor radius of j. And using formulae of Bessel function,

$$\frac{J_{n-1}(a) + J_{n+1}(a)}{2} = \frac{nJ_n(a)}{a} \tag{3.62}$$

$$\frac{J_{n-1}(a) - J_{n+1}(a)}{2} = \frac{d}{da}J_n(a) \equiv J_n'(a_j) \tag{3.63}$$

perturbed distribution function f_{j1} is written as

$$f_{j1}(\mathbf{r},\mathbf{v},t) = -\frac{q_j}{m_j}e^{i(k_x x + k_z z - \omega t)}\sum_{m,n}\Big[U_j\left(\frac{nJ_n}{a_j}\right)E_x - iU_j J_n'(a_j)E_y$$
$$+\left(W_j\left(\frac{nJ_n}{a_j}\right) + \frac{\partial f_{j0}}{\partial v_z}\right)E_z\Big]\frac{J_m\exp(i(m-n)\theta)}{i(k_z v_z - \omega - n\Omega)}. \tag{3.64}$$

Substituting Eqs.(3.64) and (3.48) into Eq.(3.47), relationship between $\mathbf{j}_1$ and $\mathbf{E}_1$ is shown. Thus we can obtain dielectric tensor of hot plasma.

$$\frac{\overleftrightarrow{\epsilon}}{\epsilon_0} = \overleftrightarrow{I} - \sum_j \frac{\omega_{pj}^2}{\omega} \sum_{n=-\infty}^{\infty} \int d^3v \overleftrightarrow{T}_{jn} \frac{v_\perp^{-1} U_j n_{j0}^{-1}}{k_z v_z - \omega - n\Omega_j} - \hat{z}\hat{z} \sum_j \frac{\omega_{pj}^2}{\omega}^2 \left(1 + \frac{1}{n_{j0}} \int d^3v \frac{v_z^2}{v_\perp} \frac{\partial f_{j0}}{\partial v_\perp}\right) \tag{3.65}$$

$$\overleftrightarrow{T}_{jn} = \begin{pmatrix} v_\perp^2 \left(\frac{nJ_n}{a_j}\right)^2 & iv_\perp^2 \left(\frac{nJ_n}{a_j}\right) J_n' & -v_\perp v_z \left(\frac{nJ_n}{a_j}\right) J_n \\ -iv_\perp^2 \left(\frac{nJ_n}{a_j}\right) J_n' & v_\perp^2 \left(J_n'\right)^2 & iv_\perp v_z J_n' J_n \\ -v_\perp v_z \left(\frac{nJ_n}{a_j}\right) J_n & -iv_\perp v_z J_n' J_n & v_z^2 J_n^2 \end{pmatrix} \tag{3.66}$$

Substituting Eq.(3.65) into Eq.(3.26), we can obtain dispersion relation of hot plasma wave. However, it is hard to understand the property of hot plasma wave from Eq.(3.65).

3.2.2 Dispersion Relation of Hot Wave for Maxwell Distribution

Considering the case f_{j0} is bi-Maxwellian,

$$f_{j0} = n_{j0} F_\perp(v_\perp) F_z(V_z) \tag{3.67}$$

$$F_\perp(v_\perp) = \frac{m_j}{2\pi\kappa T_\perp} \exp\left[-\frac{mv_\perp^2}{2\kappa T_\perp}\right] \tag{3.68}$$

$$F_z(V_z) = \sqrt{\frac{m_j}{2\pi\kappa T_\perp}} \exp\left[-\frac{m(v_z - V)^2}{2\kappa T_z}\right] \tag{3.69}$$

we can simplify Eq.(3.65) as follows, i.e. we can integrate dielectric tensor in velocity space analytically.

$$\frac{\overleftrightarrow{\epsilon}}{\epsilon_0} = \overleftrightarrow{I} + \sum_j \frac{\omega_{pj}^2}{\omega^2} \left(\sum_{n=-\infty}^{\infty} \left[\left(\zeta_{j0} Z(\zeta_{jn}) - \left(1 - \frac{1}{R_T}\right) \left(1 + \zeta_{jn} Z(\zeta_{jn})\right) \right) e^{-\lambda_j} \overleftrightarrow{X}_{jn} \right] + 2\eta_{j0}^2 R_T \hat{z}\hat{z} \right) \tag{3.70}$$

Then

$$\overleftrightarrow{X}_{jn} = \begin{pmatrix} n^2 \frac{I_n}{\lambda_j} & in(I_n' - I_n) & -(2R_T)^{1/2} \eta_{jn} \frac{n}{\alpha_j} I_n \\ -in(I_n' - I_n) & \left(\frac{n^2}{\lambda_j} + 2\lambda_j\right) I_n - 2\lambda_j I_n' & i(2R_T)^{1/2} \eta_{jn} \alpha_j (I_n' - I_n) \\ -(2R_T)^{1/2} \eta_{jn} \frac{n}{\alpha_j} I_n & -i(2R_T)^{1/2} \eta_{jn} \alpha_j (I_n' - I_n) & 2R_T \eta_{jn}^2 I_n \end{pmatrix} \tag{3.71}$$

$$\eta_{jn} \frac{\omega - n\Omega_j}{\sqrt{2} k_z v_{jT_z}} \tag{3.72}$$

$$R_T = \frac{T_z}{T_\perp} \tag{3.73}$$

$$\lambda_j = \alpha_j^2 = \left(\frac{k_\perp v_{jT_\perp}}{\Omega_j} \right)^2 \tag{3.74}$$

$$v_{jT_{z,\perp}} = \frac{\kappa T_{z,\perp}}{m_j} \tag{3.75}$$

and $Z(\zeta_{jn})$ is the plasma dispersion function [18].

$$Z(\zeta_{jn}) = \begin{cases} \pi^{-1/2} \displaystyle\int_{-\infty}^{\infty} d\beta \frac{\exp[-\beta^2]}{\beta - \zeta_{jn}} & (\mathrm{Im}[\omega] > 0) \\ \pi^{-1/2} \displaystyle\int_{-\infty}^{\infty} d\beta \frac{\exp[-\beta^2]}{\beta - \zeta_{jn}} + i \frac{k_z}{|k_z|} \pi^{1/2} \exp[-\zeta_{jn}^2] & (\mathrm{Im}[\omega] = 0) \\ \pi^{-1/2} \displaystyle\int_{-\infty}^{\infty} d\beta \frac{\exp[-\beta^2]}{\beta - \zeta_{jn}} + 2i \frac{k_z}{|k_z|} \pi^{1/2} \exp[-\zeta_{jn}^2] & (\mathrm{Im}[\omega] =< 0) \end{cases} \tag{3.76}$$

$$\zeta_{jn} = \frac{\omega - k_z V - n\Omega_j}{k_z \sqrt{\dfrac{2\kappa T_z}{m_j}}} \tag{3.77}$$

3.2.3 Dispersion Relation of Electron Bernstein Wave

Consider the case where the wave is electrostatic. In this case, wave equation Eq.(3.26) is converted to more simple form, i.e. operate $\mathbf{n}\cdot$ from left of both side of Eq.(3.26) and use $\mathbf{E}_1 \parallel \mathbf{k}$.

$$\mathbf{n} \cdot \overleftrightarrow{\epsilon} \cdot \mathbf{n} = 0$$

$$\Rightarrow n_x^2 \epsilon_{xx} + 2 n_x n_z \epsilon_{xz} + n_z^2 \epsilon_{zz} = 0 \tag{3.78}$$

Eq.(3.78) gives the dispersion relation of electrostatic wave. Assume f_{j0} is bi-Maxwellian again and the case where the wave propagates perpendicular to magnetic field. Such wave, i.e. electrostatic wave, propagates perpendicular to magnetic field and hot plasma wave, is called Electron Bernstein Wave (EBW) which is discovered first by I.B.Bernstein[2]. In the case, dispersion relation Eq.(3.78) becomes more simple form.

$$\epsilon_{xx} = 0 \tag{3.79}$$

Here we use ϵ_{xx} of Eq.(3.70). And for simplicity, assuming no flow velocity along magnetic field exists (V=0), temperatures of each direction (parallel and perpendicular) are same ($T_z = T_\perp$) and the frequency of wave is so large that ions cannot respond, we can obtain the dispersion relation of EBW.

$$1 + \frac{\omega_{pe}^2}{\Omega_e^2} \frac{1}{\lambda_e} \left[1 - \sum_{n=-\infty}^{\infty} \frac{\omega}{\omega - n\Omega_e} e^{-\lambda_e} I_n \right] \tag{3.80}$$

Here $k_z \sim 0$ is considered, thus we used asymptotic form of plasma dispersion function.

$$Z(\zeta_{jn}) \sim -\frac{1}{\zeta_{jn}} + i\pi^{1/2}\sigma \exp(-\zeta_{jn}^2) \tag{3.81}$$

$$\sigma = \begin{cases} 0 & |\mathrm{Im}[\zeta_{jn}]| > |\mathrm{Re}[\zeta_{jn}]|, \mathrm{Im}[\zeta_{jn}] > 0 \\ 1 & |\mathrm{Im}[\zeta_{jn}]| < |\mathrm{Re}[\zeta_{jn}]| \\ 2 & |\mathrm{Im}[\zeta_{jn}]| > |\mathrm{Re}[\zeta_{jn}]|, \mathrm{Im}[\zeta_{jn}] < 0 \end{cases} \tag{3.82}$$

The second term of Eq.(3.81) is usually negligible small. However at nth harmonic of ECR, it is important for calculation of absorption to leave this term.

3.3 Mode Conversion to Electron Bernstein Wave

In the previous section, dispersion relation of EBW is derivated. Since EBW is an electrostatic wave, it cannot propagate in the vacuum. Thus something method to convert from electromagnetic wave to EBW is needed.

3.3.1 Principle of Mode Conversion to Electron Bernstein Wave

It is well known that there are three methods to convert EMW to EBW.

- Perpendicular injection of X-Wave from high field side (SX-B Conversion)
- Perpendicular injection of X-Wave from low field side (FX-SX-B Conversion)
- Oblique injection of O-Wave from low field side (O-X-B Conversion)

Figure 3.1 shows an example of radial profile of electron density and Table 3.1 shows the condition of this experiment.

The perpendicular refractive index of O-Wave and X-Wave are drawn in Fig.3.2 and that of EBW is drawn in Fig.3.3. And Fig.3.4 shows refractive indices of both X-Wave and EBW at the vicinity of Upper Hybrid Resonance (UHR) Layer. Eq. (3.80) is transformed into

$$\left(\frac{\Omega_e}{\omega_{pe}}\right)^2 = \frac{\alpha(q, \lambda_e)}{\lambda_e} \tag{3.83}$$

$$q \equiv \frac{\omega}{\Omega_e} \tag{3.84}$$

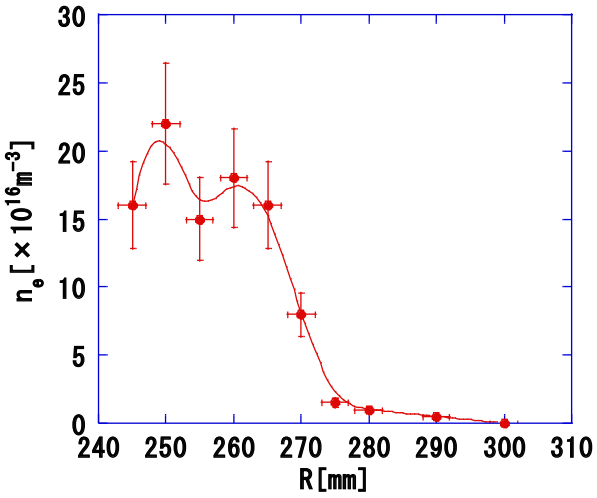

Table 3.1: Condition of Experiment

F-Coil	40mm Levitated
Configuration	Regular
Current F-Coil / L-Coil	35kA / 15kA
Filling Pressure of H_2	1.5×10^{-3}Pa
Measurement Equipment	Double Probe

Figure 3.1: Radial Profile of Electron Density

$$\alpha(q, \lambda_e) \equiv 2 \sum_{n=1}^{\infty} e^{-\lambda_e} I_n(\lambda_e) \frac{n^2}{q^2 - n^2}. \tag{3.85}$$

Considering the case where the $k_\perp \rho_e \ll 1$,

$$e^{\lambda_e} \sim 1, I_1 \sim \frac{\lambda_e}{2}, I_{n \geq 2} \sim 0 \tag{3.86}$$

the dispersion relation of EBW in this case is written as

$$\left(\frac{\Omega_e}{\omega_{pe}} \right)^2 = \frac{1}{q^2 - 1}, \tag{3.87}$$

thus

$$\omega^2 = \omega_{pe}^2 + \Omega_2^2 = \omega_{UH}^2. \tag{3.88}$$

Therefore $k_\perp \rho_e$ approaches to zero at UHR [19].

The refractive index of X-Wave goes to infinity at UHR and, at there, cold plasma approximation falls. On the other hand, the refractive index of EBW approaches zero. The mode conversion process may occur at UHR. It is necessary to send X-Wave to UHR. Figure 3.6 is the CMA diagram which shows the normal surface of the wave (This figure is quotation from Ref.[20]). In this figure horizontal axis corresponds plasma density normalized by incident wave's frequency. Vertical axis corresponds magnetic field strength normalized by incident wave's frequency. Solid lines represent various resonance condition and doted lines represent various cutoff condition. If the incident wave is launched out of plasma, initial position of incident wave on the CMA diagram is a spot on the vertical axis.

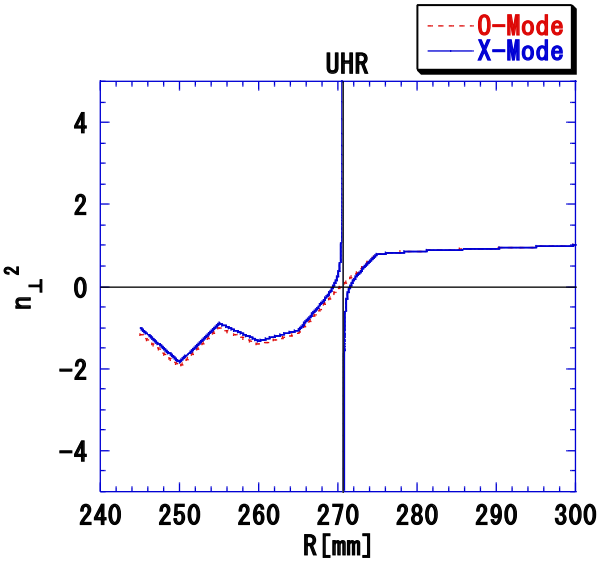

Figure 3.2: Refractive Index of Cold Waves

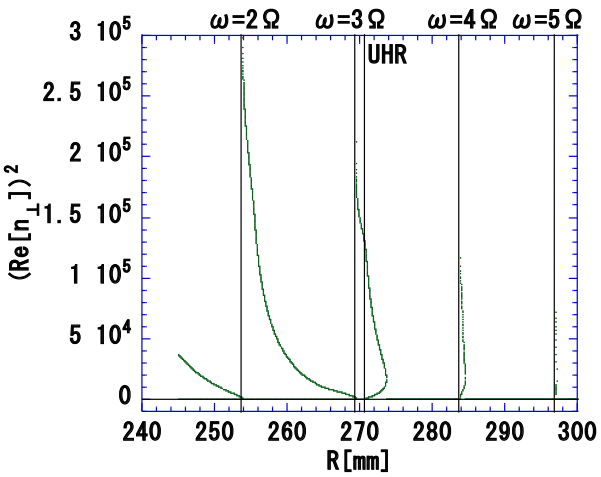

Figure 3.3: Refractive Index of EBW

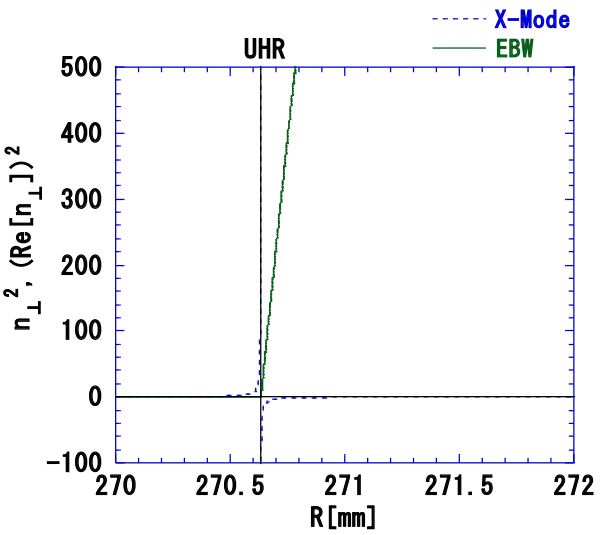

Figure 3.4: Refractive indices at the vicinity of UHR

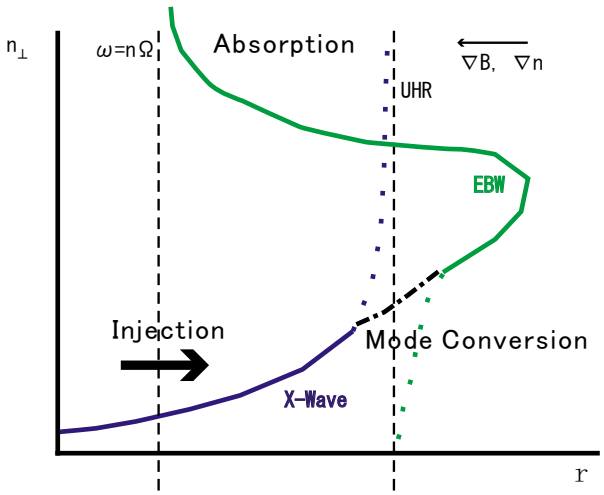

Figure 3.5: Schematic Drawing of SX-B Conversion

Figure 3.5 shows the schematic drawing of SX-B conversion. This is the simplest method in principle, however this method is technically difficult.

FX-SX-B conversion is an available method, which is drawn in Fig.3.7. Launched Fast X-Wave propagates from high field side to low field side and approaches to Right Hand Cutoff (R-Cutoff). If the evanescent region is sufficiently thin, i.e. density or magnetic field varies steeply, the tunnelling of the incident Fast X-Wave occurs and Slow X-Wave reaches to Left Hand Cutoff (L-Cutoff). Slow X-Wave is reflected backward to UHR where Slow X-Wave converted to EBW as well as SX-B conversion.

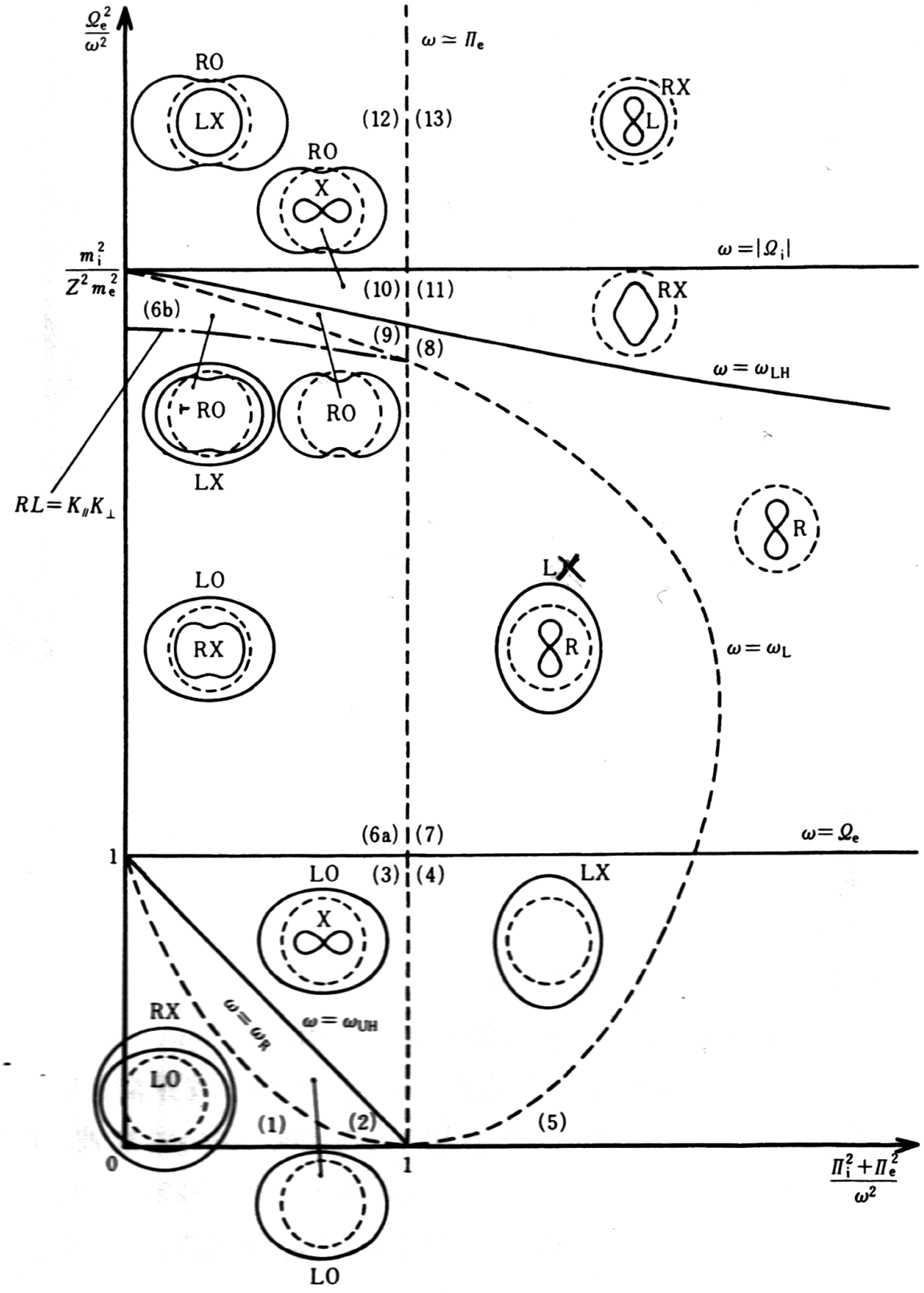

Figure 3.6: CMA Diagram

O-X-B conversion is also available method, which is drawn in Fig.3.8. Launched slow O-Wave propagates from low field side to high field side and this wave passes through R-Cutoff and UHR and reaches to plasma cutoff (P-Cutoff). If the positions of O-Wave's P-Cutoff and X-Wave's L-Cutoff overlap, mode conversion from O-Wave to X-Wave occurs. And converted X-Wave propagates to UHR and converted to EBW there. Note that in this case definition of L-Cutoff is

$$n_{\parallel}^2 = L \tag{3.89}$$

here L is defined in Eq.(3.20). This means X-wave cannot propagate to high field side along magnetic field. Thus parallel component of refractive index at cutoff layer has to be optimized.

$$n_{\parallel opt}^2 = \frac{\Omega_e}{\omega + \Omega_e} \tag{3.90}$$

Optimization of launch angle is not easy since required condition is given as Eq.(3.90).

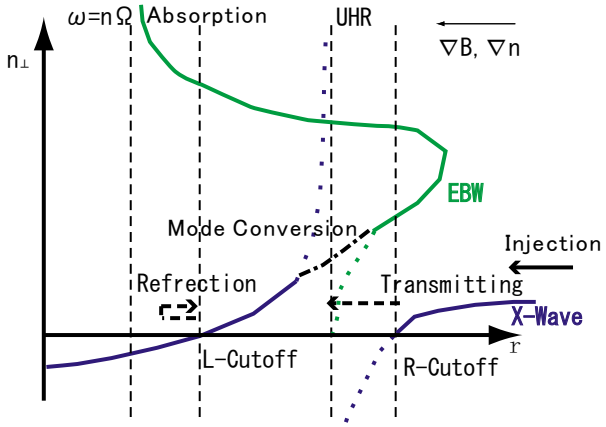

Figure 3.7: Schematic Drawing of FX-SX-B Conversion

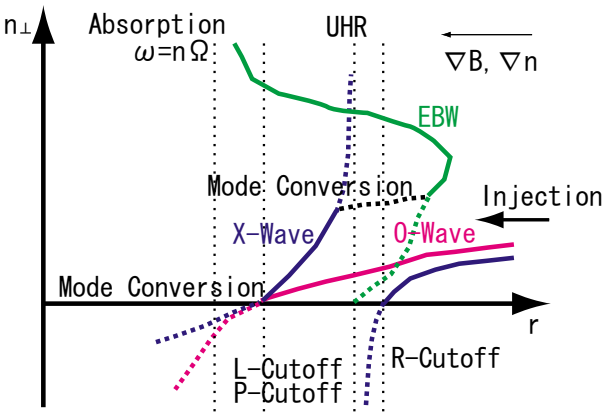

Figure 3.8: Schematic Drawing of O-X-B Conversion

Trajectory on the CMA diagram of each three method of mode conversion is drawn in Figs.3.9, 3.10 and 3.11. As shown in Fig.3.10 X-Wave is accessible in the case of FX-SX-B conversion only if X-Wave passes through the evanescent region which lies between R-Cutoff and UHR.

3.3.2 Conversion Efficiency

In this section theories of mode conversion efficiency with X-Wave injection from low field side are reviewed. Consideration of O-X-B conversion on Mini-RT will be needed.

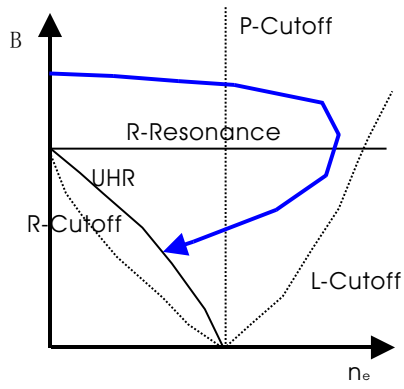

Figure 3.9: Trajectory on CMA Diagram of SX-B Conversion

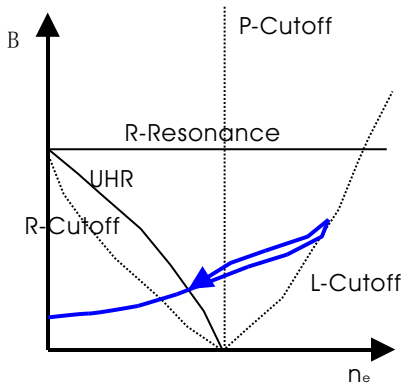

Figure 3.10: Trajectory on CMA Diagram of FX-SX-B Conversion

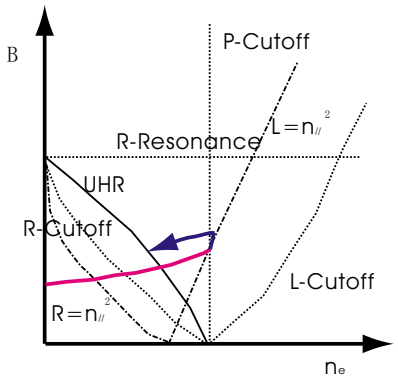

Figure 3.11: Trajectory on CMA Diagram of O-X-B Conversion

However it is difficult (but not impossible) to optimize launch angle and O-Wave injection experiments were not carried out circumstantially in this study.

Conversion efficiency from electromagnetic waves to EBW are function of density, magnetic field strength and gradient of these. K.G. Budden carried out study of mode conversion efficiency [21]. He constructed a model of refractive index at the vicinity of UHR. And analytical solution is obtained, i.e. Whittaker function which is one of confluent hypergeometric function.

Equation (3.27) changes the form by assuming perpendicular propagation ($\cos\theta = 0$, $\mathbf{k} \parallel \hat{x}$), inhomogeneity in the x-direction and uniformity in the y-direction.

$$\frac{d^2 E_y}{d\xi^2} + \Phi(\xi) E_y = 0 \tag{3.91}$$

Here

$$\xi \equiv \frac{\omega x}{c} \tag{3.92}$$

$$\Phi(\xi) \equiv \frac{S^2 - D^2}{S} \tag{3.93}$$

where S and D are defined in Eq.(3.17)-(3.20). K.G. Budden made the model of $\Phi(\xi)$ which is called potential function and approximately corresponds to the square of refractive index (notation of this paper differs from that of Budden's).

$$\Phi(\xi) = \gamma - \frac{\beta}{\xi} \tag{3.94}$$

This model represents that the location of UHR corresponds to $\xi =$ and $\sqrt{\gamma}$ corresponds to $n_\perp$ for sufficiently large ξ. And location of R-Cutoff is at $\xi = \beta/\gamma$. Refractive index of

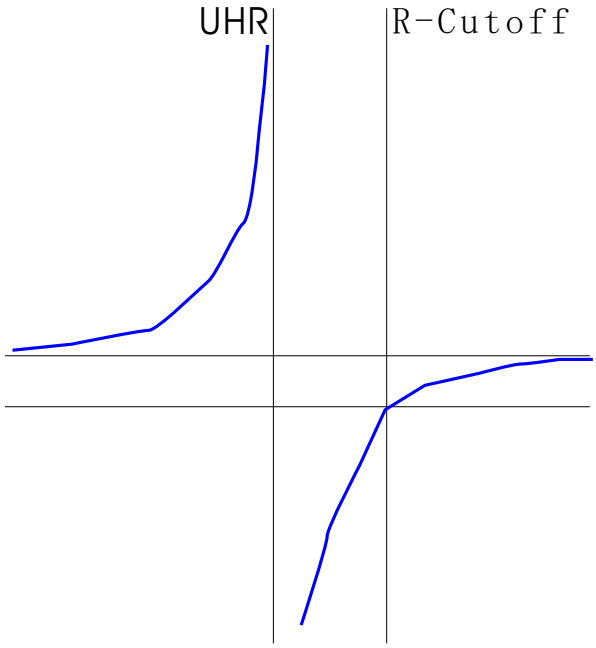

Figure 3.12: Refractive index of X-Wave modeled by Budden

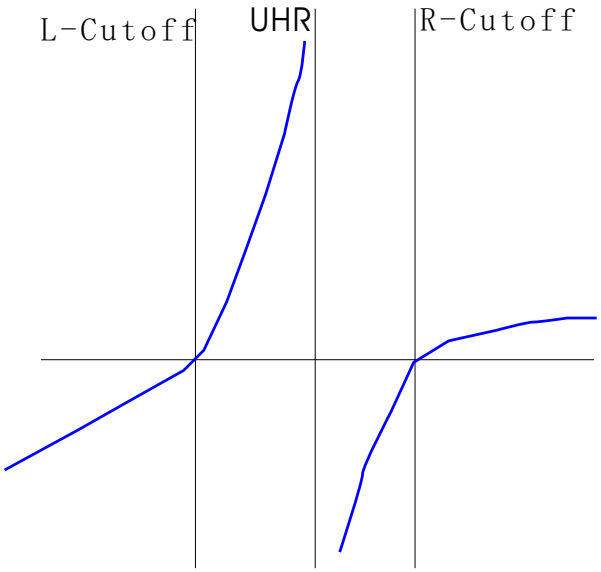

Figure 3.13: Refractive index of X-Wave modeled by Ram

X-wave modeled by K.G. Budden is shown in Fig.3.12. By defining as follows

$$\zeta \equiv 2i\sqrt{\gamma}\xi \tag{3.95}$$

$$-\frac{i}{2}\frac{\beta}{\sqrt{\gamma}} \equiv -\frac{i}{2}\eta \equiv \kappa \tag{3.96}$$

Eq.(3.91) changes the form to

$$\frac{d^2E_y}{d\zeta} + \left(-\frac{1}{4} - \frac{i\eta/2}{\zeta}\right)E_y = 0. \tag{3.97}$$

Equation (3.97) is the special case of Whittaker differential equation. General solutions of Eq.(3.97) are

$$E_y = c_1 W_{\kappa,1/2}(\zeta) + c_2 W_{-\kappa,-1/2}(-\zeta) \tag{3.98}$$

where c_1 and c_2 are arbitrary constants which depend on boundary conditions. Function W are the Whittaker functions[22].

To investigate the mode conversion efficiency, asymptotic form of Whittaker functions $W_{\kappa,\mu}(\zeta)$ are used. For $\xi \to \infty$

$$W_{\kappa,1/2}(\zeta) \sim \zeta^{\kappa}\mathrm{e}^{-z/2} = |2\sqrt{\gamma}\xi|^{-i\eta/2}\mathrm{e}^{-\pi\eta/4}\mathrm{e}^{i\sqrt{\gamma}\xi} \tag{3.99}$$

$$W_{-\kappa,1/2}(-\zeta) \sim \left(\zeta^{-\kappa}\mathrm{e}^{z/2} - \frac{2\pi i}{\Gamma(\frac{1}{2}-\mu+\kappa)\Gamma(\frac{1}{2}+\mu+\kappa)}\zeta^{\kappa}\mathrm{e}^{-\zeta/2}\right)\mathrm{e}^{i\pi\kappa}$$
$$= |2\sqrt{\gamma}\xi|^{i\eta/2}\mathrm{e}^{3\pi\eta/4}\mathrm{e}^{-i\sqrt{\gamma}\xi} - \frac{2\pi i}{\Gamma(-i\eta/2)\Gamma(1-i\eta/2)}|2\sqrt{\gamma}\xi|^{-i\eta/2}\mathrm{e}^{\pi\eta/4}\mathrm{e}^{i\sqrt{\gamma}\xi} \tag{3.100}$$

and for $\xi \to -\infty$

$$W_{\kappa,1/2}(\zeta) \sim \zeta^{\kappa} \mathrm{e}^{-\zeta/2} = |2\sqrt{\gamma}\xi|^{-i\eta/2} \mathrm{e}^{\pi\eta/4} \mathrm{e}^{-i\sqrt{\gamma}\xi} \tag{3.101}$$

$$W_{-\kappa,1/2}(-\zeta) \sim \zeta^{-\kappa} \mathrm{e}^{i\pi\kappa} \mathrm{e}^{\zeta/2} = |2\sqrt{\gamma\xi}|^{i\eta/2} \mathrm{e}^{\pi\eta/4} \mathrm{e}^{-i\sqrt{\gamma}\xi} \tag{3.102}$$

Note that we assumed time dependence of the form $\exp(-i\omega t)$. Thus for $\xi \to \infty$, $W_{\kappa,1/2}(\zeta)$ represents an incoming wave (toward $\xi = 0$) while $W_{-\kappa,1/2}(-\zeta)$ represents an outgoing wave. For $\xi \to -\infty$, $W_{\kappa,1/2}(\zeta)$ represents an outgoing wave while $W_{-\kappa,1/2}(-\zeta)$ represents combination of an incoming wave and an outgoing wave. In this model, relevant solution to Eq.(3.97) is $W_{-\kappa,1/2}(-\zeta)$ because of no source of wave at $\xi \to -\infty$.

The ratio of incident wave and reflected wave amplitude gives the reflection coefficient.

$$|R| = \frac{2\pi \exp(-\pi\eta/2)}{|\Gamma(-i\eta/2)\Gamma(1 - i\eta/2)|} = 1 - \mathrm{e}^{-\pi\eta} \tag{3.103}$$

Similarly the ratio of incident wave and transmission wave amplitude gives the transmission coefficient.

$$|T| = \mathrm{e}^{-\pi\eta/2} \tag{3.104}$$

The conversion efficiency is written as

$$C = 1 - |R^2| - |T^2| = \mathrm{e}^{-\pi\eta}(1 - \mathrm{e}^{-\pi\eta}) \tag{3.105}$$

here η is called tunnelling parameter which means the product of wave number at infinity and distance from R-Cutoff to UHR. Maximum mode conversion efficiency with Budden's model is $\frac{1}{4}$ when $|T|^2 = \frac{1}{2}$.

A.K. Ram studied excitation, propagation and damping of EBW [23][24]. In his theory the effect of reflection of transmitted X-Wave at L-Cutoff. Figure 3.13 shows the refractive index of X-Wave in his model. This method is FX-SX-B conversion. The term $\Psi(\xi)$ in Eq.(3.91) is written in Ram's model as

$$\Phi(\xi) = \begin{cases} \gamma - \dfrac{\beta}{\xi} & \xi > 0 \\ \alpha\xi + \gamma' - \dfrac{\beta}{\xi} & \xi < 0. \end{cases} \tag{3.106}$$

In this case mode conversion efficiency is written as follows.

$$C(\eta, \phi) = 4\mathrm{e}^{-\pi\eta}(1 - \mathrm{e}^{-\pi\eta}) \cos^2(\phi/2 + \theta) \tag{3.107}$$

Here θ is the phase of $\Gamma(-i\eta/2)$ and ϕ is determined by the positional relation R and L-Cutoff and UHR. In this case perfect mode conversion may occur if the following two

waves are same amplitude and phase difference is $i\pi$. One is the X-Wave reflected at R-Cutoff directly. The other is X-Wave first transmitting evanescent region second reflected at L-Cutoff and again transmitting evanescent region.

Tunnelling parameter η is important for mode conversion. Since η corresponds the distance from UHR and R-Cutoff, it is obtained by using density and magnetic field strength and these gradient length.

$$\eta = \frac{\Omega_e L_n}{c} \frac{\alpha}{\sqrt{\alpha^2 + 2(L_n/L_B)}} \left(\frac{\sqrt{1+\alpha^2} - 1}{\alpha^2 + (L_n/L_B)\sqrt{1+\alpha^2}} \right)^{1/2} \tag{3.108}$$

where $\alpha \equiv \frac{\omega_{pe}}{\Omega_e}$, $L_n \equiv \frac{n}{|dn/dr|}$ and $L_B \equiv \frac{B}{|dB/dr|}$ [23].

For example, assuming $\alpha \sim 1$, $L_n \ll L_B$ and $B = 0.1T$, we obtained the necessary condition of perfect mode conversion from Eq.(3.108), $L_n = 1.5$mm. This is the reason why FX-SX-B conversion is reasonable method on Mini-RT, i.e. B ∼0.02-0.04T and L_n ∼50mm at UHR. However note that α ∼1 and $L_n \ll L_B$ are not satisfied in Mini-RT. Conversion efficiency on Mini-RT have to be calculated without such approximation.

3.4 Absorption of Waves in Plasma

Plasma is heated by interaction between wave and plasma. Energy absorption coefficient is derived from Maxwell equations.

From the Eqs. (3.3) and (3.4)

$$\nabla \cdot \left(\mathbf{E} \times \frac{\mathbf{B}}{\mu_0} \right) + \mathbf{E} \cdot \frac{\partial \mathbf{D}}{\partial t} + \frac{1}{\mu_0} \mathbf{B} \cdot \frac{\partial \mathbf{B}}{\partial t} = 0. \tag{3.109}$$

The first term of this equation is called Poynting vector.

$$\mathbf{E} \times \frac{\mathbf{B}}{\mu_0} \equiv \mathbf{P} \tag{3.110}$$

Second and third term of (3.109) denote the electric and magnetic field energy respectively. We are interested in time averaged real part of Eq. (3.109). It is well known the time averaged value of product Re[A]Re[B] is written as

$$\overline{AB} \equiv \frac{1}{4}(A_0 B_0^* + A_0^* B_0)\exp(2\phi_i) = \frac{1}{4}(A_0 B_0^* + A_0^* B_0)\exp(2\int_\infty^t \omega_i dt') \tag{3.111}$$

here A is written

$$A = A_0 \exp\left(-i \int_{-\infty}^{t} (\omega_r + i\omega_i) dt' \right) \tag{3.112}$$

and B is similar to A.

$$B = B_0 \exp\left(-i\int_{-\infty}^{t}(\omega_r + i\omega_i)dt'\right) \tag{3.113}$$

A_0 and B_0 are any complex numbers. And ω_r and ω_i are real numbers which vary slowly. Averaging out (3.109) with respect to time over the period, time averaged conservation law is obtained.

$$\nabla \cdot \mathbf{P} + \frac{\partial W}{\partial t} = 0 \tag{3.114}$$

$$\mathbf{P} = \frac{1}{4\mu_0}(\mathbf{E}_1^* \times \mathbf{B}_1 + \mathbf{E}_1 \times \mathbf{B}_1^*)\mathrm{e}^{2\phi_i} \tag{3.115}$$

$$\frac{\partial W}{\partial t} = \left[\omega_i \frac{1}{2\mu_0}\mathbf{B}_1^* \cdot \mathbf{B}_1 + \frac{1}{2}\left(\omega_i \mathbf{E}_1^* \cdot \left(\frac{\overleftrightarrow{\epsilon} + \overleftrightarrow{\epsilon}^\dagger}{2}\right) \cdot \mathbf{E}_1 + \omega_r \mathbf{E}_1^* \cdot \left(\frac{\overleftrightarrow{\epsilon} - \overleftrightarrow{\epsilon}^\dagger}{2i}\right) \cdot \mathbf{E}_1\right)\right] \mathrm{e}^{2\phi_i} \tag{3.116}$$

The factor ω_i denotes temporal decay or amplification rate of the wave. If the third term of (3.116) is equal to zero, i.e. $\overleftrightarrow{\epsilon}$ is Hermitian, the behavior of plasma is lossfree. The effect of damping of wave which occurs even if the system is steady state is put into the third term of (3.116) (or anti-Hermitian part of dielectric tensor). Hermitian and anti-Hermitian part of dielectric tensor $\overleftrightarrow{\epsilon}_H$ and $\overleftrightarrow{\epsilon}_A$ are

$$\overleftrightarrow{\epsilon} = \left(\frac{\overleftrightarrow{\epsilon} + \overleftrightarrow{\epsilon}^\dagger}{2}\right) + i\left(\frac{\overleftrightarrow{\epsilon} - \overleftrightarrow{\epsilon}^\dagger}{2i}\right) \equiv \overleftrightarrow{\epsilon}_{\mathrm{H}} + i\overleftrightarrow{\epsilon}_{\mathrm{A}} \tag{3.117}$$

$$\epsilon_{ij}^\dagger \equiv \epsilon_{ji}^* \tag{3.118}$$

$$\overleftrightarrow{\epsilon}_{\mathrm{H}}^\dagger = \overleftrightarrow{\epsilon}_{\mathrm{H}},\ \overleftrightarrow{\epsilon}_{\mathrm{A}}^\dagger = -\overleftrightarrow{\epsilon}_{\mathrm{A}}. \tag{3.119}$$

The physical meaning of the term $\frac{\omega_r}{2}\mathbf{E}_1^* \cdot \overleftrightarrow{\epsilon}_{\mathrm{A}} \cdot \mathbf{E}_1 \equiv P_{\mathrm{ab}}$ is work per unit time and volume by electric field which are absorbed in plasma.

$$\frac{\omega_r}{2}\mathbf{E}_1^* \cdot \overleftrightarrow{\epsilon}_{\mathrm{A}} \cdot \mathbf{E}_1 = \frac{\omega_r}{2}\mathrm{Re}[\mathbf{E}_1^* \cdot (-i)\overleftrightarrow{\epsilon} \cdot \mathbf{E}_1]|_{\omega=\omega_r} = \frac{\omega_r}{2}\mathrm{Re}[\mathbf{E}_1^* \cdot \mathbf{j}]|_{\omega=\omega_r} = \omega_r\overline{\mathbf{E} \cdot \mathbf{j}} \tag{3.120}$$

Thus

$$P_{\mathrm{ab}} = \frac{\omega_r}{2}\Big(|E_x|^2\mathrm{Im}[\epsilon_{xx}] + |E_y|^2\mathrm{Im}[\epsilon_{yy}] + |E_z|^2\mathrm{Im}[\epsilon_{zz}] + 2\mathrm{Im}[E_x^*E_y]\mathrm{Re}[\epsilon_{xy}] + 2\mathrm{Im}[E_y^*E_z]\mathrm{Re}[\epsilon_{yz}] + 2\mathrm{Im}[E_z^*E_x]\mathrm{Re}[\epsilon_{xz}]\Big). \tag{3.121}$$

If plasma is perfectly cold ($k_\perp\rho_e = 0$), (3.121) is zero (see (3.16)). Thus we must consider lowest order of temperature effect to estimate the energy absorption into cold plasma. From here $\omega_i \sim 0$ is assumed.

If distribution function of plasma without perturbation is isotropic Maxwellian ($T_\parallel = T_\perp$) and no velocity along magnetic field exists ($V = 0$), dielectric tensor of hot plasma with Maxwellian (3.70) is simplified as follows.

$$\frac{\overleftrightarrow{\epsilon}}{\epsilon_0} = \overleftrightarrow{I} + \sum_j \frac{\omega_{pj}^2}{\omega^2} \left[\sum_{n=-\infty}^{\infty} \zeta_{j0} Z(\zeta_{jn}) e^{-\lambda_j} \overleftrightarrow{X}_{jn} + 2\zeta_{j0}^2 R_T \hat{z}\hat{z} \right] \tag{3.122}$$

Here $\overleftrightarrow{X}_{jn}$ changes the form to

$$\overleftrightarrow{X}_{jn} = \begin{pmatrix} n^2 \dfrac{I_n}{\lambda_j} & in(I_n' - I_n) & -2^{1/2}\zeta_{jn}\dfrac{n}{\alpha_j} I_n \\ -in(I_n' - I_n) & \left(\dfrac{n^2}{\lambda_j} + 2\lambda_j\right) I_n - 2\lambda_j I_n' & i2^{1/2}\zeta_{jn}\alpha_j(I_n' - I_n) \\ -2^{1/2}\zeta_{jn}\dfrac{n}{\alpha_j} I_n & -i2^{1/2}\zeta_{jn}\alpha_j(I_n' - I_n) & 2\zeta_{jn}^2 I_n \end{pmatrix}. \tag{3.123}$$

Expanding modified Bessel function and $\mathrm{e}^{-\lambda_j}$

$$\begin{aligned} I_n(\lambda_j) &= \left(\frac{\lambda_j}{2}\right)^n \sum_{l=0}^{\infty} \frac{1}{l!(n+l)!} \left(\frac{\lambda_j}{2}\right)^{2l} \\ &= \left(\frac{\lambda_j}{2}\right)^n \left(\frac{1}{n!} + \frac{1}{1!(n+1)!}\left(\frac{\lambda_j}{2}\right)^2 + \frac{1}{2!(n+2)!}\left(\frac{\lambda_j}{2}\right)^4 + \cdots \right) \end{aligned} \tag{3.124}$$

$$\mathrm{e}^{-\lambda_j} = 1 - \lambda_j + \frac{1}{2}\lambda_j^2 + \cdots . \tag{3.125}$$

Each component of dielectric tensor is as follows.

$$\frac{\epsilon_{xx}}{\epsilon_0} = 1 + \sum_j X_j \zeta_{j0} \left[(Z_1 + Z_{-1}) \left(\frac{1}{2} - \frac{\lambda_j}{2} + \cdots \right) + (Z_2 + Z_{-2}) \left(\frac{\lambda_j}{2} - \lambda_j^2 + \cdots \right) + \cdots \right] \tag{3.126}$$

$$\begin{aligned} \frac{\epsilon_{yy}}{\epsilon_0} = 1 + \sum_j X_j \zeta_{j0} \Big[& Z_0(2\lambda_j + \cdots) + (Z_1 + Z_{-1}) \left(\frac{1}{2} - \frac{3\lambda_j}{2} + \cdots \right) \\ & + (Z_2 + Z_{-2}) \left(\frac{\lambda_j}{2} - \lambda_j^2 + \cdots \right) + \cdots \Big] \end{aligned} \tag{3.127}$$

$$\begin{aligned} \frac{\epsilon_{zz}}{\epsilon_0} = 1 - \sum_j X_j \zeta_{j0} \Big[& 2\zeta_{j0} W_0 (1 - \lambda_j + \cdots) + (\zeta_{j1} W_1 + \zeta_{j,-1} W_{-1})(b + \cdots) \\ & + (\zeta_{j2} W_2 + \zeta_{j,-2} W_{-2}) \left(\frac{\lambda_j^2}{4} + \cdots \right) + \cdots \Big] \end{aligned} \tag{3.128}$$

$$\frac{\epsilon_{xy}}{\epsilon_0} = -\frac{\epsilon_{yx}}{\epsilon_0} = i \sum_j X_j \zeta_{j0} \left[(Z_1 + Z_{-1}) \left(\frac{1}{2} - \lambda_j + \cdots \right) + (Z_2 + Z_{-2}) \left(\frac{\lambda_j}{2} + \cdots \right) + \cdots \right] \tag{3.129}$$

$$\frac{\epsilon_{xz}}{\epsilon_0} = \frac{\epsilon_{zx}}{\epsilon_0} = 2^{1/2} \sum_j X_j \lambda_j \zeta_{j0} \left[(W_1 - W_{-1}) \left(\frac{1}{2} + \cdots \right) + (W_2 - W_{-2}) \left(\frac{\lambda_j}{4} + \cdots \right) + \cdots \right] \tag{3.130}$$

$$\frac{\epsilon_{yz}}{\epsilon_0} = -\frac{\epsilon_{zy}}{\epsilon_0} = 2^{1/2} \sum_j X_j \lambda_j^{1/2} \zeta_{j0} \Big[\zeta_{j0} W_0 \left(-1 + \frac{3\lambda_j}{2} + \cdots \right)$$
$$+ (W_1 + W_{-1}) \left(\frac{1}{2} + \cdots \right) + (W_2 - W_{-2}) \left(\frac{\lambda_j}{4} + \cdots \right) + \cdots \Big] \tag{3.131}$$

$$Z_n \equiv Z(\zeta_n) \tag{3.132}$$

$$W_n \equiv -(1 + \zeta_n Z_n) \tag{3.133}$$

$$\zeta_n \equiv \frac{\omega - n\Omega_j}{2^{1/2} k_z \left(\frac{\kappa T_z}{m_j} \right)^{1/2}} \tag{3.134}$$

$$X_j \equiv \left(\frac{\omega_{pj}}{\omega} \right)^2 \tag{3.135}$$

In the case of electron cyclotron heating, contribution from ion can be neglected. Absorption by nth harmonic of ECR is determined by the term attributed to $\zeta_{e0} Z_{-n}$. Assuming $\lambda_e \ll 1$, Eqs.(3.126)-(3.131) are rewritten simply as

$$\mathrm{Im}[\epsilon_{xx,-n}] = \mathrm{Im}[\epsilon_{yy,-n}] = \epsilon_0 (\omega_{pe}/\omega)^2 G_{-n} \alpha_n \tag{3.136}$$

$$\mathrm{Im}[\epsilon_{zz,-n}] = \epsilon_0 (\omega_{pe}/\omega)^2 2\zeta_{-n}^2 G_{-n} \lambda_e \alpha_n n^{-2} \tag{3.137}$$

$$\mathrm{Re}[\epsilon_{xy,-n}] = \epsilon_0 (\omega_{pe}/\omega)^2 G_{-n} \alpha_n \tag{3.138}$$

$$\mathrm{Re}[\epsilon_{yz,-n}] = -\epsilon_0 (\omega_{pe}/\omega)^2 (2\lambda_e)^{1/2} \zeta_{-n} G_{-n} \alpha_n n^{-1} \tag{3.139}$$

$$\mathrm{Re}[\epsilon_{xz,-n}] = \epsilon_0 (\omega_{pe}/\omega)^2 (2\lambda_e)^{1/2} \zeta_{-n} G_{-n} \alpha_n n^{-1} \tag{3.140}$$

where

$$\alpha_n \equiv \frac{n^2}{2 \cdot n!} (\lambda_e/2)^{n-1} \tag{3.141}$$

$$G_{-n} \equiv \mathrm{Im}[\zeta_0 Z_{-n}] = \frac{k_z}{|k_z|} \pi^{1/2} \zeta_0 \exp(-\zeta_{-n}^2). \tag{3.142}$$

Thus Eq.(3.121) changes the form to

$$P_{ab,-n} = \frac{1}{2} \omega \left(\frac{\omega_{pe}}{\omega} \right)^2 G_{-n} \alpha_n |E_x - i E_y|^2 \tag{3.143}$$

As shown in Eq.(3.142) wave's energy is sufficiently absorbed only the resonance condition $\omega - n\Omega_e = 0$ is satisfied where n is any negative integer.

On Mini-RT, typical electron temperature and magnetic field strength are 10eV and 0.05T respectively. In this case, $\lambda_e \sim 10^{-4}$ for X-Wave is satisfied except to the vicinity of UHR. Thus absorption caused by 2nd, 3rd, 4th, $\cdots$ cyclotron damping drops extremely rapid with the harmonic number n increasing.

On the other hand the refractive index of EBW diverges at any harmonic ECR. The parameter $\lambda_e \ll 1$ is not satisfied there. Thus EBW is absorbed sufficiently even if electron temperature is low. If electron temperature is locally high at one of the harmonics of ECR, it suggests the heating by EBW which is converted at UHR. Cutoff of electron Bernstein wave also occurs at any nth harmonic of ECR. Electron Bernstein wave can propagate particular region, i.e. nth and $(n+1)$th ECR. This is the reason why a particular harmonic number of ECR location is heated by EBW.

Chapter 4

Experimental Setup

4.1 Detector System

4.1.1 Double Probe

Double probe is a kind of the electrostatic probe which has two probes. This measurement method can be applied even if the reference voltage does not exist. Figure 4.1 shows the drawing of Double probe and Fig.4.2 is the photograph of the head of Double probe.

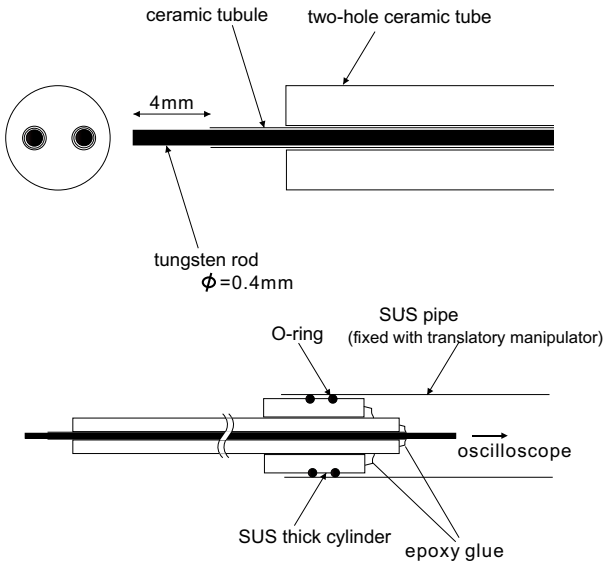

Figure 4.1: Drawing of Double Probe Used on Mini-RT

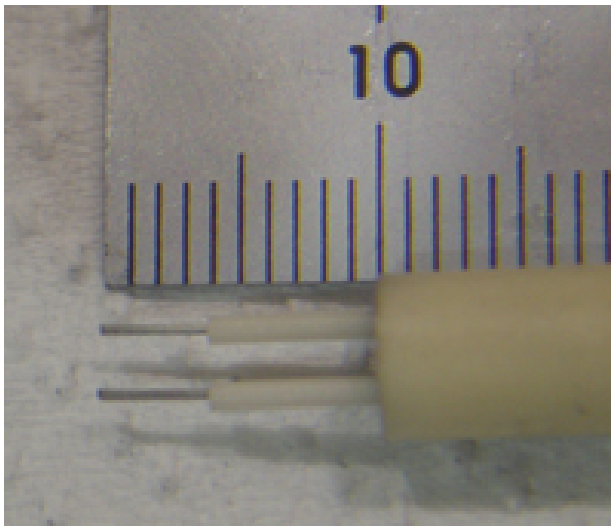

Figure 4.2: Double Probe Head

Probe tips are made of tungsten (cylindrical shape, ϕ=4mm), which is covered with

ceramic tube for insulation. These tungsten rods are inserted in the two-hole ceramic tube and fixed by epoxy glue for vacuum seal. And two-hole ceramic tube is also fixed with SUS thick cylinder by epoxy glue. And SUS thick cylinder is fixed with SUS pipe by O-ring. The SUS pipe is fixed with translatory manipulator.

Figure 4.3 and Table 4.1 show the schematic drawing of Double Probe circuit and characteristic values of plasma. Voltage between the two probes are swept ±120V by

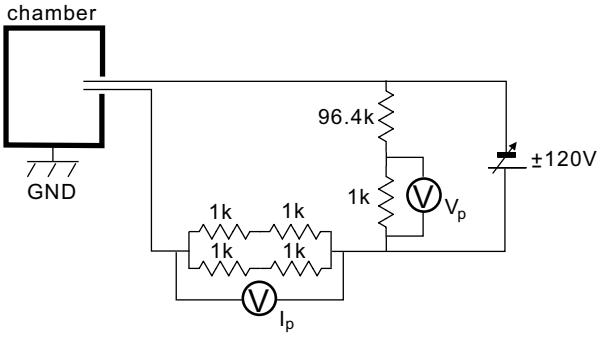

Figure 4.3: Schematic Drawing of Double Probe Circuit

Table 4.1: Characteristic Values of Plasma

Electron Density	$5.0 \times 10^{16}\mathrm{m}^{-3}$
Electron Temperature	10 eV
Ion Temperature	0.5 eV
Magnetic Field	0.05 T
Debye Length	$1.1 \times 10^{-4}\mathrm{m}$
Electron Larmor Radius	$2.1 \times 10^{-4}\mathrm{m}$
Ion Larmor Radius	$2.0 \times 10^{-3}\mathrm{m}$
Ion Sound Speed	$3.1 \times 10^{4}\mathrm{m/s}$

a bipolar power supply. Current from plasma is measured as a voltage signal along a resistor.

Since the shape of probe is cylindrical, the current does not saturate even if enough voltage ($> \dfrac{\kappa T_e}{e}$) is applied. Figure 4.4 shows the typical i-v characteristic and our method to estimate the ion saturation current and electron temperature. Relationship of electron density n_e, electron temperature T_e, ion saturation current I_{is} and V_c is

$$T_e[eV] = \frac{V_c}{2} \tag{4.1}$$

$$I_{is} = 0.61 e^{3/2} n_e \sqrt{\frac{T_e[eV]}{m_i}} S. \tag{4.2}$$

Here e and S denote the elemental charge and surface area of probe.

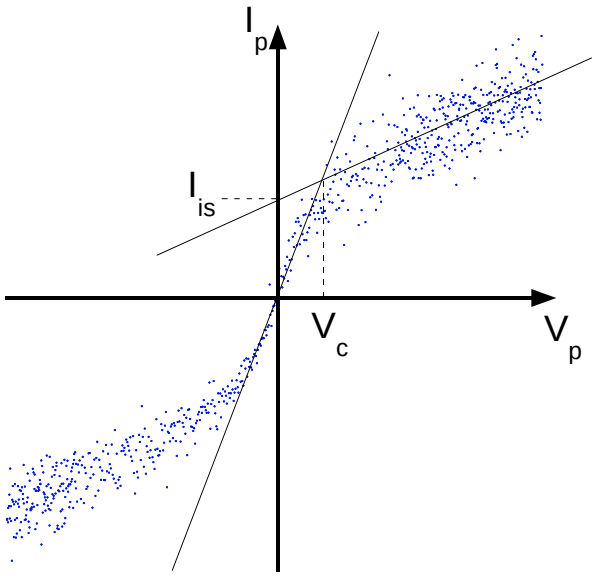

Figure 4.4: Typical i-v Characteristic

4.1.2 Triple Probe

Triple probe is also an electrostatic probe which has three or more probes. Triple probe is marked by the ability to measure electron temperature and electron density without sweeping the bias voltage. Thus it enables to high time resolution measurement.

Triple Probe used on Mini-RT has four probes. Figure 4.5 and Fig.4.6 show the circuit of Triple Probe and head of Triple Probe respectively. Potential differences between each probe and chamber are measured. Fourth probe is a dummy for keeping symmetry. Applied bias voltage is DC 90V and on the other hand measured electric temperature is 5∼20eV.

Lower two probes in Fig.4.5 are used for measurement of floating potential. The simplified drawing of triple probe circuit is shown in Fig. 4.7. One of a probes is electrically floated from the ground. Other two probes are also floated and connected with low impedance and biased by DC power supply. Figure 4.8 shows the relationship between current into probe and potential of probe. We set reference potential is the space potential of plasma and positive direction of current is equivalent to flow of electron.

Since high impedance resister is used, current into probe tip 2 is very small, thus $V_2 = V_f$. And same reason, current into tip 1 is opposite to that into tip 3.

$$I_2 = I_1 - I_3 = 0 \tag{4.3}$$

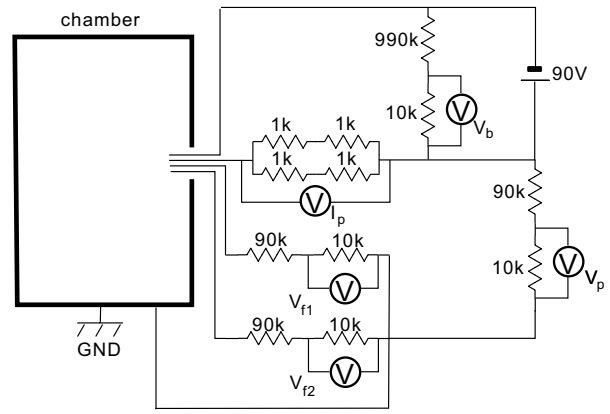

Figure 4.5: Schematic Drawing of Triple Probe Circuit

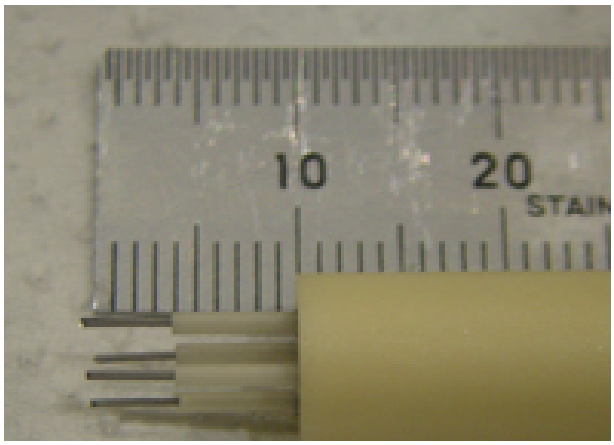

Figure 4.6: Triple Probe Head

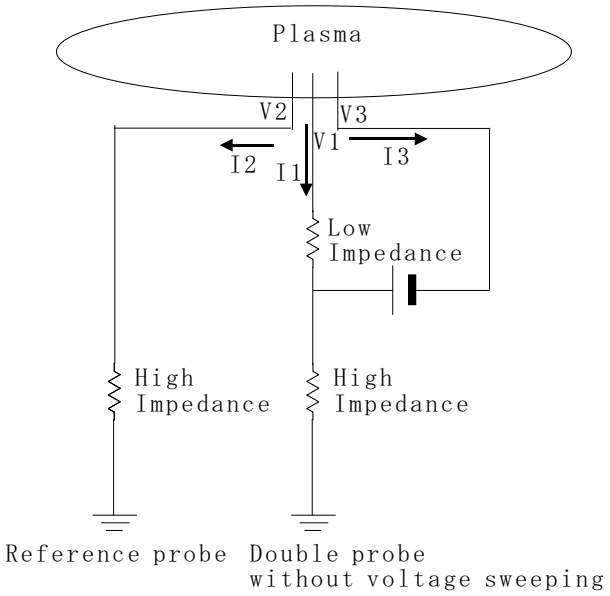

Figure 4.7: Simplified Drawing of Triple Probe Circuit

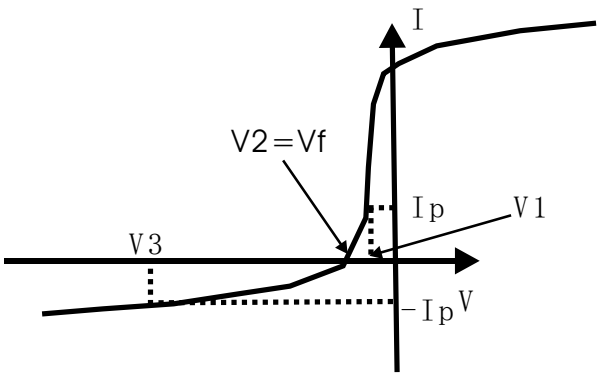

Figure 4.8: i-v Characteristic

Potential of three probes are negative unless DC bias voltage is extremely high. Thus current contributed by ion equals to ion saturation current. We assume electron distribution function follows Boltzmann distribution. Electron currents are

$$I_{e,k} = I_{e0} \mathrm{e}^{\phi_k}. \tag{4.4}$$

Here subscript k denotes probe tip's number and I_{e0} denotes electron current when probe potential equals to plasma potential. Variable ϕ_k is defined as

$$\phi_k \equiv \frac{V_k}{T_e} \tag{4.5}$$

where V_k denotes probe k's potential and T_e is in eV. Thus eq.(4.3) changes the form to

$$I_{is} - I_{e0}\mathrm{e}^{-\phi_2} = 0 \tag{4.6}$$

$$I_{e0}\mathrm{e}^{-\phi_1} - I_{e0}\mathrm{e}^{-\phi_3} = 0. \tag{4.7}$$

Transforming Eqs.(4.6) and (4.7) relation between I_1 (probe current) and I_{is} (ion saturation current) is obtained.

$$I_{is} = \frac{I_1}{1 - \mathrm{e}^{-(\phi_1 - \phi_f)}} \tag{4.8}$$

Electron density is obtained by using Eq.(4.2). Electron temperature is also obtained from I_1, I_2 and I_3

$$\frac{I_1 - I_2}{I_1 - I_3} = \frac{1}{2} = \frac{\mathrm{e}^{-\phi_1} - \mathrm{e}^{-\phi_2}}{\mathrm{e}^{-\phi_1} - \mathrm{e}^{-\phi_3}} = \frac{\mathrm{e}^{\phi_1 - \phi_f} - 1}{\mathrm{e}^{\phi_b} - 1} \tag{4.9}$$

here $\phi_b \equiv \dfrac{V_b}{T_e}$ and V_b is bias voltage.

4.1.3 75GHz Microwave Interferometer

Microwave interferometer is the device which is used for line integrated electron density measurement almost without perturbation. There is a difficulty of analysis of measured data. The range of integral is the path between transmitter and receiver of interferometer. However we would rather know averaged electron density than integrated electron density. Estimation of plasma size is very important. Especially when the F-Coil is levitated the plasma confinement region is determined by separatorix. We use the result of calculation of magnetic flux surface to estimate the plasma size.

Figure 4.9 is a photograph of transmitter horn attached on tangential port (ICF203). Transmitter horn can move back and forth by linear guide stage.

Since the frequency of incident microwave is sufficiently high (75GHz), ion cannot keep up with oscillation of electric field. Thus contribution from electron determines the refractive index. The polarization of microwave used on Mini-RT is X. In this case refractive index is approximately

$$n^2 = \frac{(\omega^2 - \omega_{pe}^2)^2 - \omega^2\Omega_e^2\sin^2\theta}{\omega^2(\omega^2 - \omega_{pe}^2) - \omega^2\omega_{pe}^2\sin^2\theta} \tag{4.10}$$

here θ denotes the angle between magnetic field and wave vector. Dropping more than second order term of $\left(\dfrac{\omega_{pe}}{\omega}\right)^2$ and $\left(\dfrac{\Omega_e}{\omega}\right)^2$, n is simplified as follows.

$$n = \sqrt{1 - \frac{\omega_{pe}^2}{\omega^2}} \sim 1 - \frac{\omega_{pe}^2}{\omega^2} \tag{4.11}$$

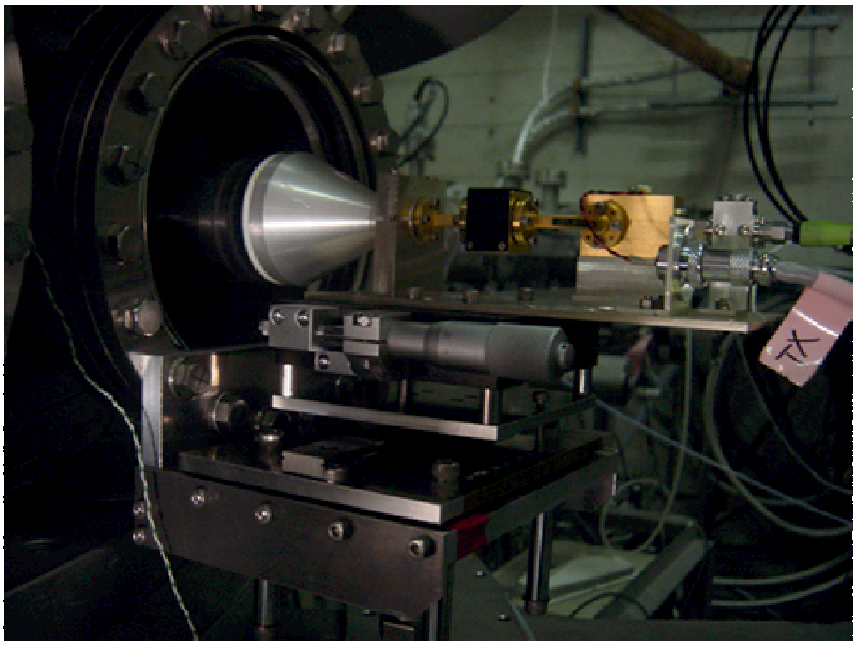

Figure 4.9: photograph of transmitter horn attached on tangential port

Eq.(4.11) gives the line integrated electron density.

$$\int n_e dx = \frac{\Delta\phi}{2\pi} \frac{8\pi^2 \epsilon_0 m_e c^2}{e^2 \lambda} \tag{4.12}$$

Here λ and $\Delta\phi$ denote wavelength of incident microwave and phase variance of the microwave which propagates plasma respectively.

Figure 4.10 shows the circuit diagram of 75GHz microwave interferometer. The interferometer consists of main unit, transmission system and receive system. Phase shift $\Delta\phi$ is detected as the voltage signal which is proportional to $\cos\Delta\phi$ by mixing the waves of signal and reference path.

4.2 Alignment of Detectors

Figure 4.11 shows the alignment of detectors on Mini-RT. Double probe and triple probe are attached on horizontal port and these move back and forth by linear translator. Measurement of electron density and electron temperature profiles are carried out shot by shot.

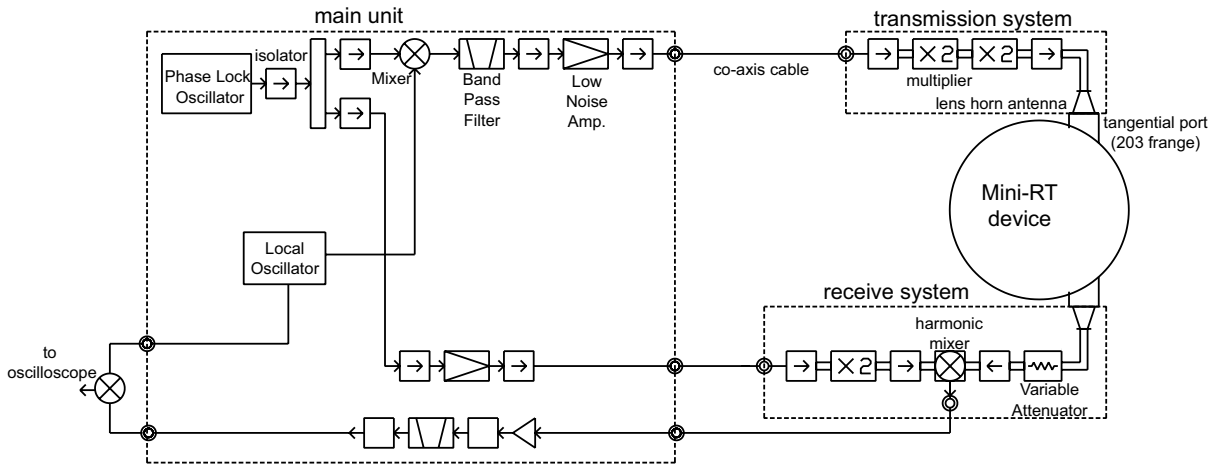

Figure 4.10: Circuit Diagram of Interferometer

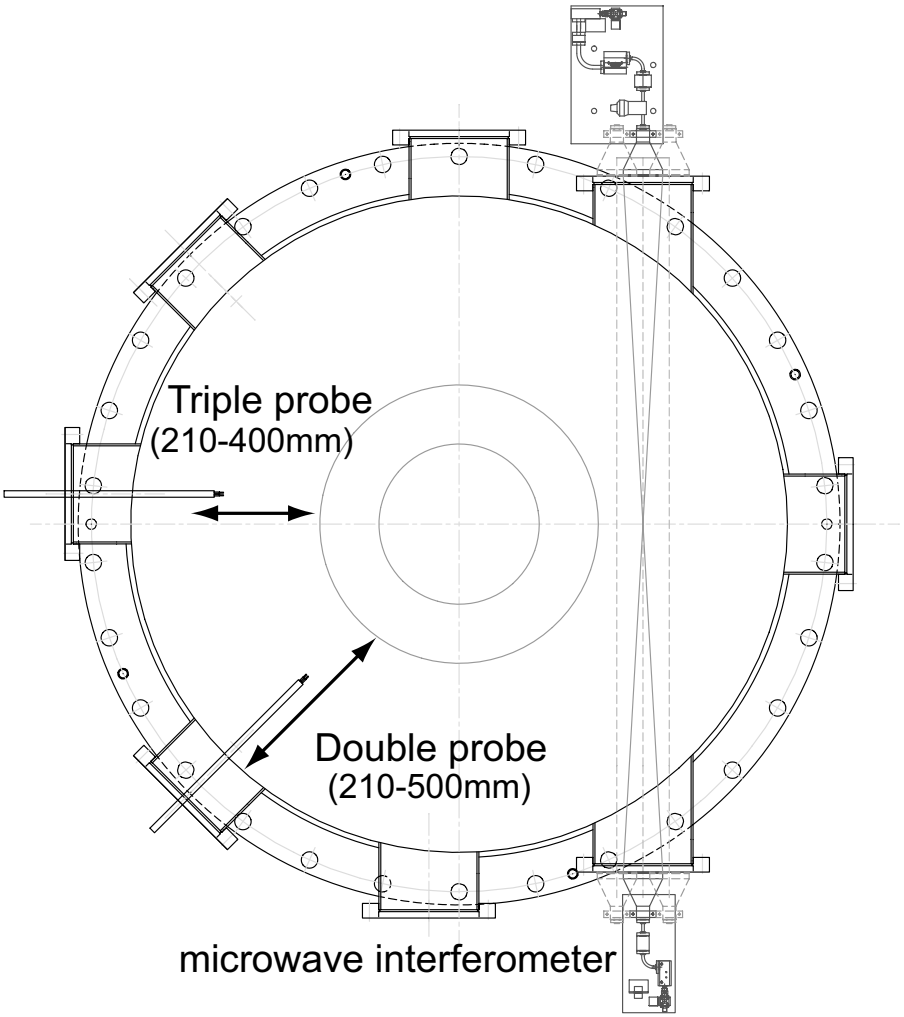

Figure 4.11: Alignment of Detectors on Mini-RT

4.3 Objective of each Experiments

All experiments of this study is carried out to investigate the possibility of heating by EBW. Mode conversion occurs at UHR surface and conversion efficiency is determined

by density, magnetic field strength and gradient of these. The location of UHR surface of cold X-Wave depends on density, magnetic field strength and frequency of incident wave. The frequency of incident wave is fixed (2.45GHz), which is in the electron cyclotron range of frequency.

To move the location of UHR by increasing and decreasing of magnitude of density profile, the power of incident wave varies. The gradient of density is varied by applying L-Coil current since plasma is confined in last closed flux surface which is determined by separatorix.

4.4 Calibration of each Detectors

Calibration of three detectors (Double probe, Triple probe, Microwave interferometer) was carried out. Microwave interferometer can avoid giving perturbation to plasma however its spatial resolution of interferometer is inferior to those of electrostatic probes. In this study results of probe measurement is mainly used since we want to know the electron density or temperature at a point.

Microwave interferometer itself was calibrated by using dielectric sheet whose permittivity was known. As shown in Figs.4.9 and 4.11, interferometer on Mini-RT is attached on tangential port. However interferometer cannot move up to the edge of device. We integrated local electron density measured by electrostatic probe along the path of microwave of interferometer and compared it with line integrated electron density measured by interferometer, on the other hand, inverse Abel transformation, i.e. local density is calculated from integrated density, is used on many devices. Figures 4.12 and 4.13 show an example of electron density profile measured by triple probe and drawing of integral method. Integrating along the path of interferometer, we obtained line integrated electron density $\int n_e dx = 1.2 \times 10^{16}\mathrm{m}^2$ for double probe and $\int n_e dx = 3.3 \times 10^{16}\mathrm{m}^2$ for triple probe. Calculation of integrated electron density was carried out as follows

$$\int n_e dx = 2 \sum_i [\{\frac{n_e(\theta_i) - n_e(\theta_{i-1})}{2}\}\{r_{i-1}\cos(\theta_{i-1}) - r_i \cos(\theta_i)\}] \tag{4.13}$$

where r_i denoted radial position at which electrostatic probes measured. The argument θ_i is defined as $\theta_i \equiv \sin^{-1}\frac{r_i}{L}$. And integrated electron density obtained by interferometer was $\int n_e dx = 3.0 \times 10^{16}\mathrm{m}^2$. Thus consistency between triple probe and interferometer measurements is sufficiently satisfied. However double probe measurement does not conform

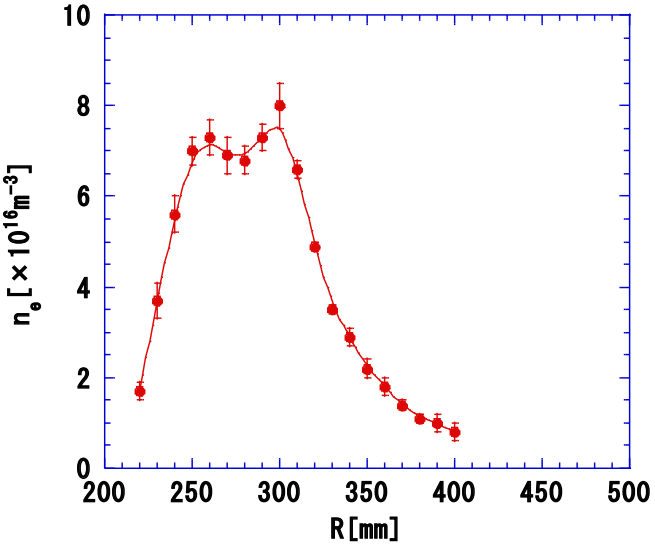

Figure 4.12: Radial Profile of Electron Density

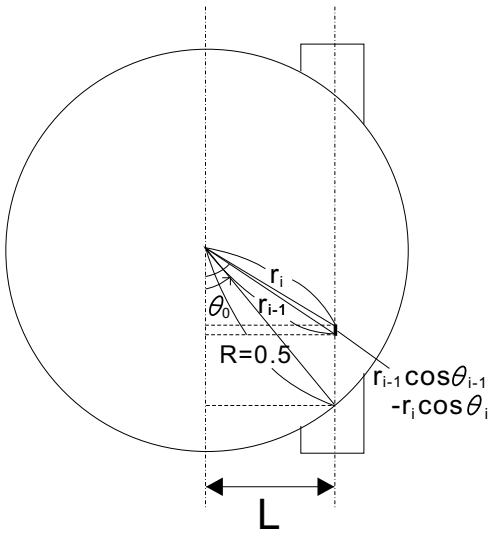

Figure 4.13: Drawing of Integral Method

to interferometer. These properties are reproducible for various magnetic configuration as long as the F-Coil is supported. If the F-Coil is levitated, the integrated electron density is different from that of interferometer.

Chapter 5

Experimental Results

5.1 Profile Measurements

5.1.1 Magnetic Configuration Dependence

Figure 5.1-5.3 show the magnetic configuration when we set the experimental condition as Table 5.1. Changing the magnetic field configuration leads to changing of the location of last closed flux surface.

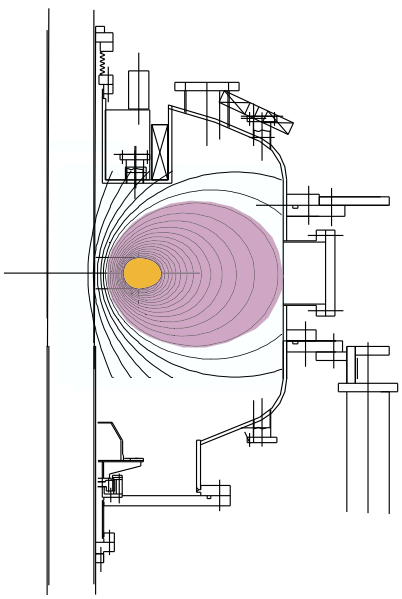

Figure 5.1: Magnetic Configuration with $I_L = 0A$

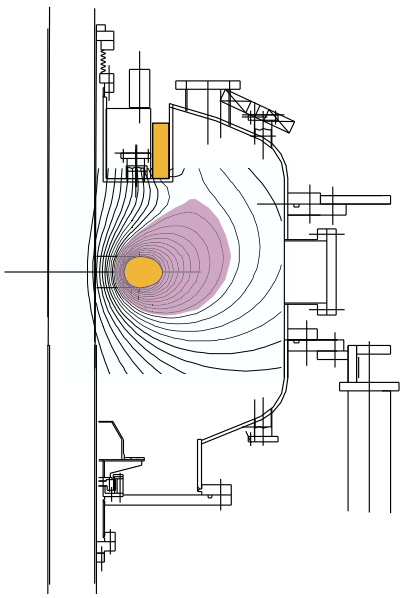

Figure 5.2: Magnetic Configuration with $I_L = 6.8kA$

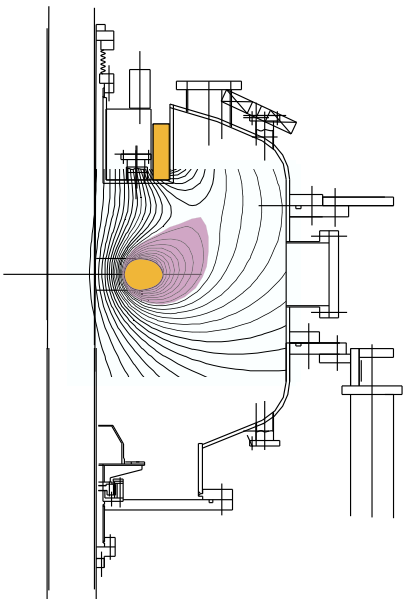

Figure 5.3: Magnetic Configuration with $I_L = 13.6kA$

Table 5.1: Experimental Condition

ECH Frequency	2.45GHz
ECH Power	2.8kW , 2sec
Incident Mode	X
Filling Pressure of H_2	4.0×10^{-2}Pa
Base Pressure	$\sim 6.0 \times 10^{-6}$Pa
Levitation of F-Coil	0mm(Supported)
Current of F-Coil	31±2kA
Current of L-Coil	0, 6.8, 13.6kA
LCFS on Midplane of Chamber	R= 500, 370, 310mm

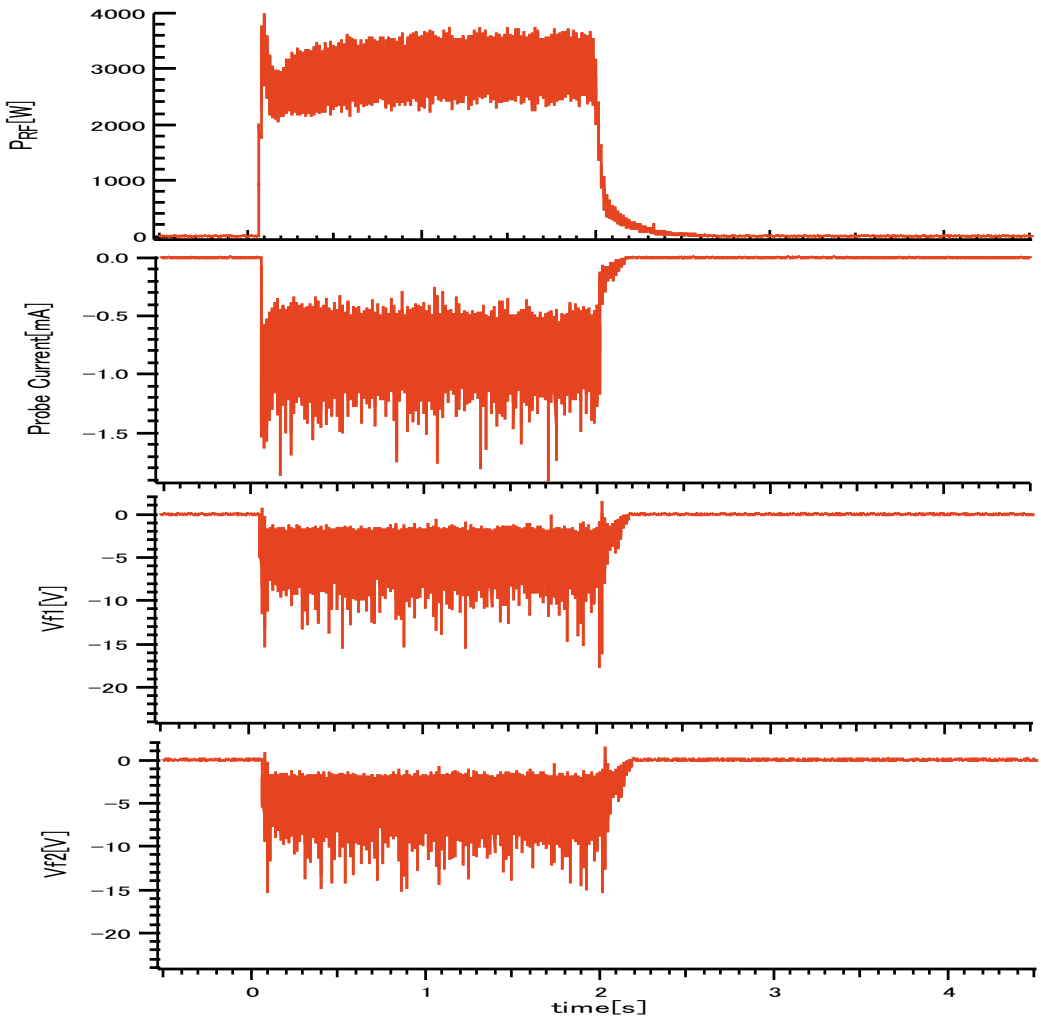

Figure 5.4: Typical Waveform

Figure 5.4 shows the typical waveform of ECH power, probe current and floating potential measured by triple probe. The signal of two probes are very similar. This means that toroidal symmetric property is approximately satisfied.

Radial profiles of electron density and electron temperature measured by triple probe are shown in Fig.5.5 and 5.6 respectively. For each configuration, peak values of electron

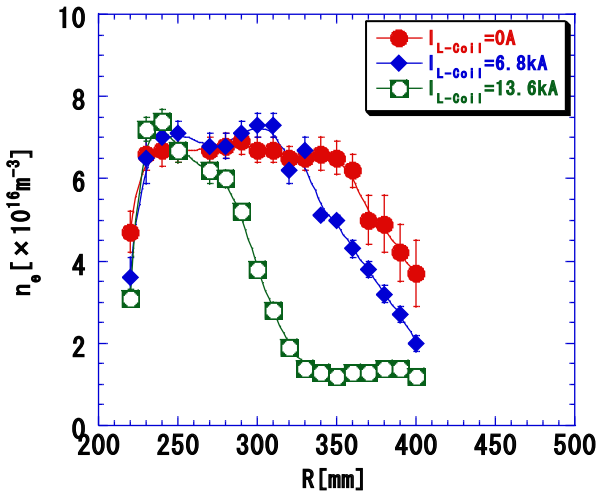

Figure 5.5: Radial Profile of Electron Density

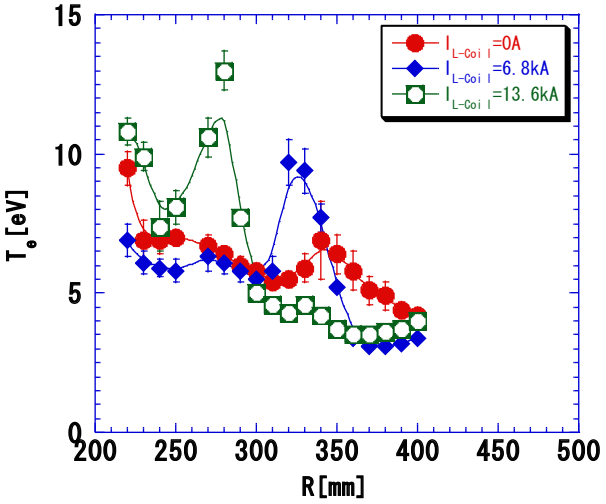

Figure 5.6: Radial Profile of Electron Temperature

density are comparable with cutoff density of 2.45GHz and O-Mode electromagnetic wave. At the vicinity of LCFS electron density gradient is steep ($L_n \sim 50$ to 100cm). And local maximum of electron temperature (LMET) exists near the top of electron density slope however in the case of I_F =0A, it does not exceed the range of error bar.

To investigate more detailed behavior, we changed the L-Coil current during discharge and secured triple probe at $R = 300$mm. Figure5.7 shows the waveform of ECH injection power, L-Coil current and floating potential. Floating potential which corresponds to electron temperature is increased at $I_L \sim 10$kA. This gives suggestions that electron temperature also depends on magnetic configuration and possibility of heating by EBW.

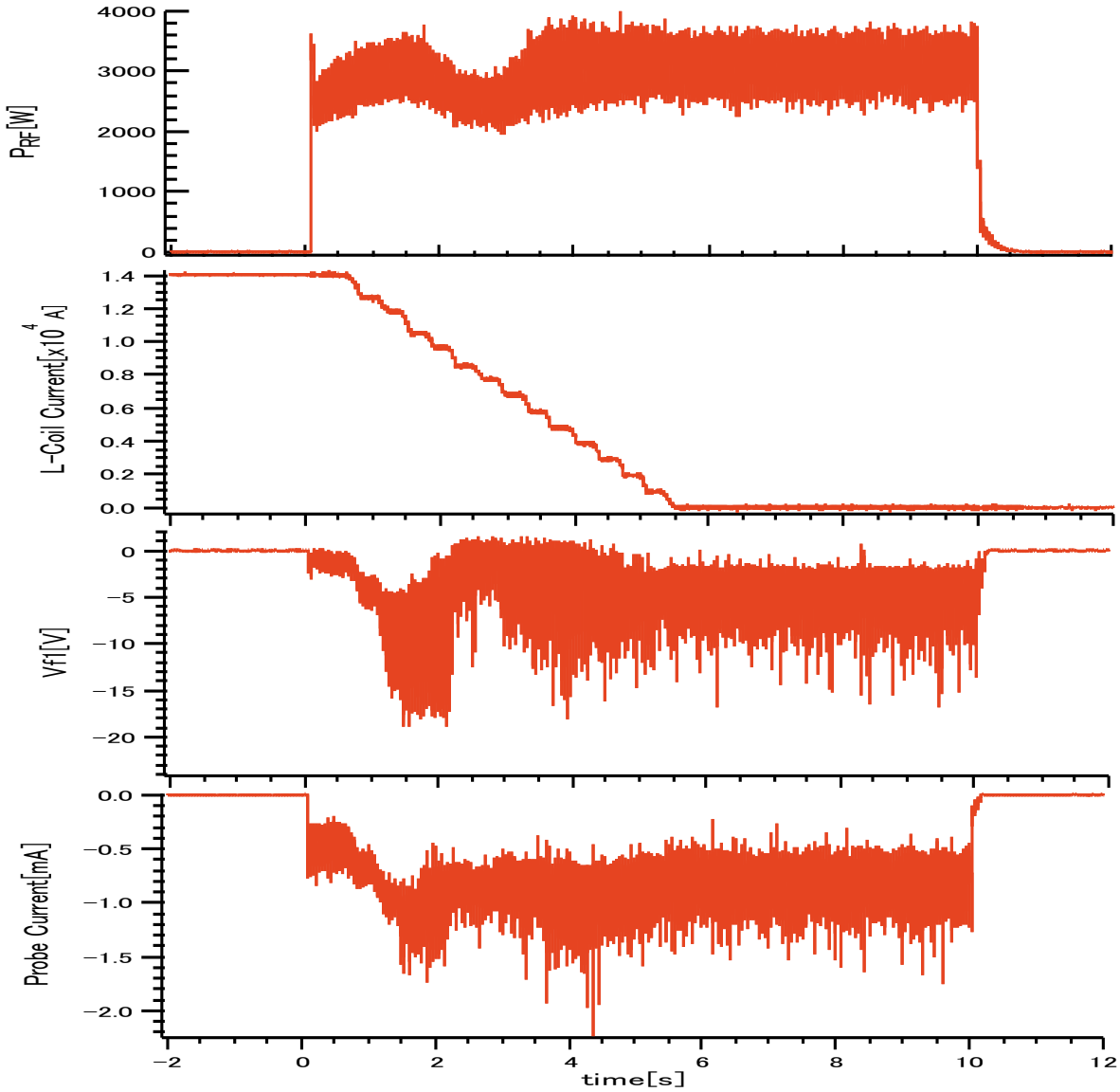

Figure 5.7: Waveform with Variation of L-Coil Current

5.1.2 Incident Power Dependence

As formulated in the section 3.3.2, conversion efficiency to EBW depends on density, magnetic strength and these characteristic gradient length. Changing the power of incident wave, we can increase and decrease the profiles of electron density. Table 5.2 shows the experimental condition and Figs.5.8 and 5.9 show the results of electron density and electron temperature profiles respectively. Electron density increases as increasing of incident power. On the other hand, electron temperature almost independent of the incident power. If the heating by EBW occurs, LMET may appear only the cases that UHR exists. In this configuration no local maximum exceeding the range of error bar exists.

Table 5.2: Experimental Condition

ECH Frequency	2.45GHz
ECH Power	0.8, 1.8, 2.8kW , 2sec
Incident Mode	X
Filling Pressure of H_2	4.0×10^{-2}Pa
Base Pressure	$\sim 6.0 \times 10^{-6}$Pa
Levitation of F-Coil	0mm(Supported)
Current of F-Coil	32±3kA
Current of L-Coil	0A, 6.8kA, 13.6kA

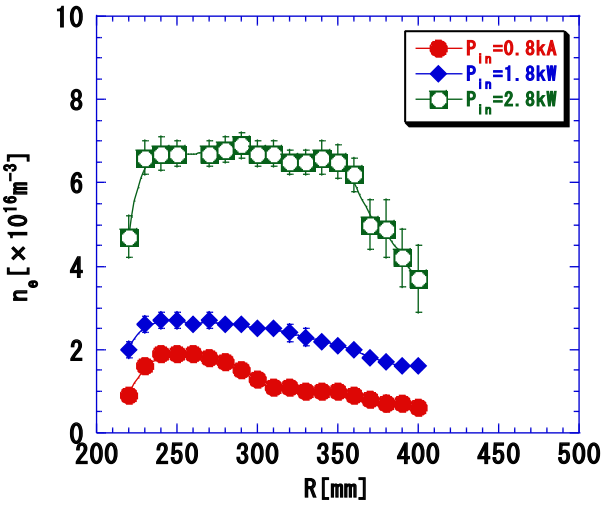

Figure 5.8: Electron Density Profile Versus Incident Power

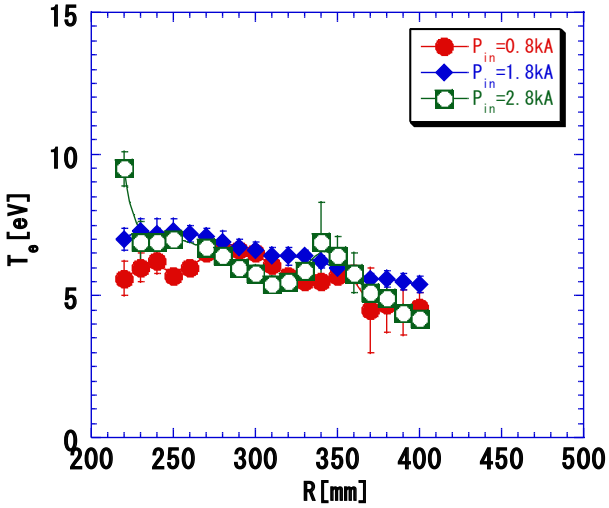

Figure 5.9: Electron Temperature Profile Versus Incident Power

To create the slope of electron density, similar experiments are carried out with energization of L-Coil current. Figures 5.10 and 5.11 show incident power dependence of electron density and electron temperature profiles with I_L =6.8kA. Similarly Figs.5.12 and 5.13 show profiles in the case with I_L =13.6kA. For each configuration, three of electron density slopes exist at roughly same position. On the other hand, LMET only notably exists for the case where electron density is high comparable with cutoff density of O-Mode.

The reason why density and temperature fluctuation becomes large when $P_{\rm in}$ =1.8kW, I_L=6.8kA is unknown. However this is the reproducible phenomenon even if electrostatic probe is not inserted into the plasma core. Figure 5.14 shows the waveforms of ECH

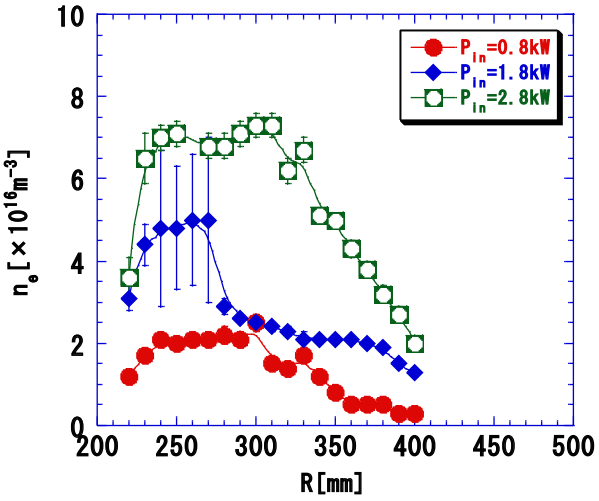

Figure 5.10: Electron Density Profile Versus Incident Power with I_L =6.8kA

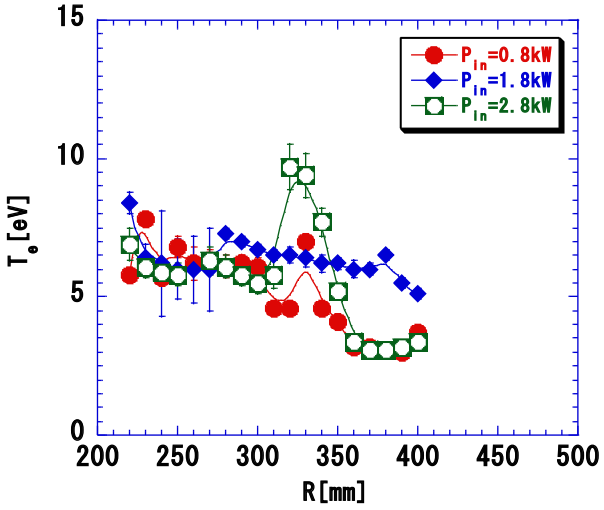

Figure 5.11: Electron Temperature Profile Versus Incident Power with I_L =6.8kA

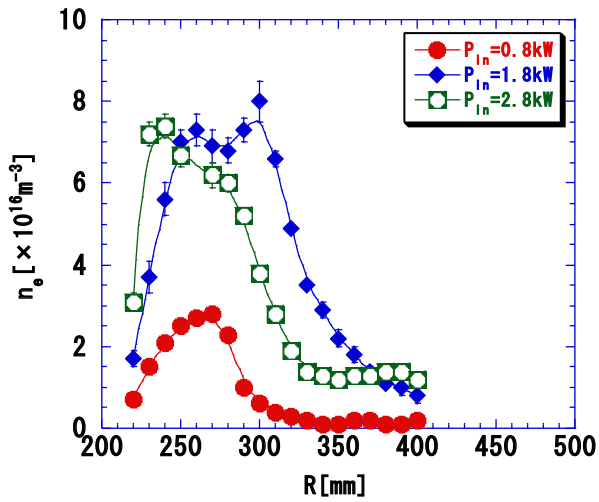

Figure 5.12: Electron Density Profile Versus Incident Power with I_L =13.6kA

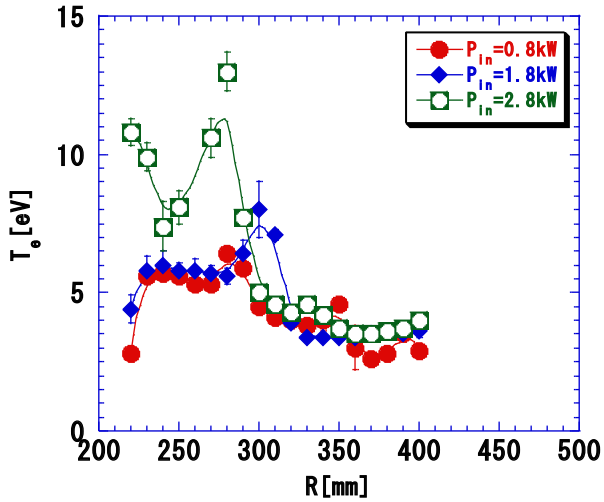

Figure 5.13: Electron Temperature Profile Versus Incident Power with I_L =13.6kA

injection power and output voltage of interferometer. When this discharge was operated, double probe and triple probe were at R =390mm.

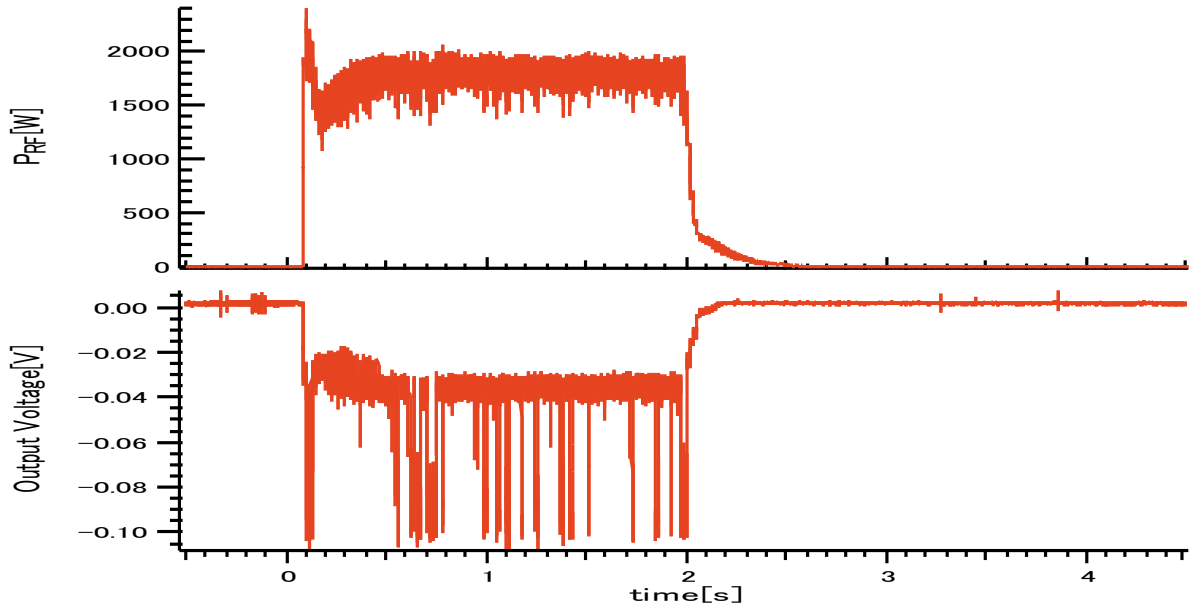

Figure 5.14: Waveform of Density Fluctuation Measured with Microwave Interferometer

5.1.3 X-Wave Injection with Internal Coil Levitated

Overdense plasma was generated by levitating F-Coil. Table 5.3 shows the experimental condition.

Table 5.3: Experimental Condition

ECH Frequency	2.45GHz
ECH Power	2.4kW 0.5sec
Incident Mode	X
Filling Pressure of H_2	4.0×10^{-3}Pa
Base Pressure	$\sim 6.0 \times 10^{-6}$Pa
Levitation of F-Coil	32mm
Current of F-Coil	41±1kA
Current of L-Coil	15.8±0.2kA

Since the multiple conditions are different from the experiments with F-Coil supported, we cannot compare the results simply. However the obvious differences between the experiments with F-Coil levitated and supported exist.

- When F-Coil is levitated, plasma generation under the lower filling gas pressure becomes possible in spite of smaller confinement region. (6.0×10^{-3}Pa for supported

and 2.0×10^{-3}Pa for levitated)

- Typical electron density and electron temperature rise twice as those of experiments with F-Coil supported respectively.
- Time constant of electron density decay becomes longer when F-Coil is levitated (however cause of this may be plasma generation under the lower filling gas pressure).

Figures 5.15 and 5.16 show profiles of electron density and electron temperature. Peak

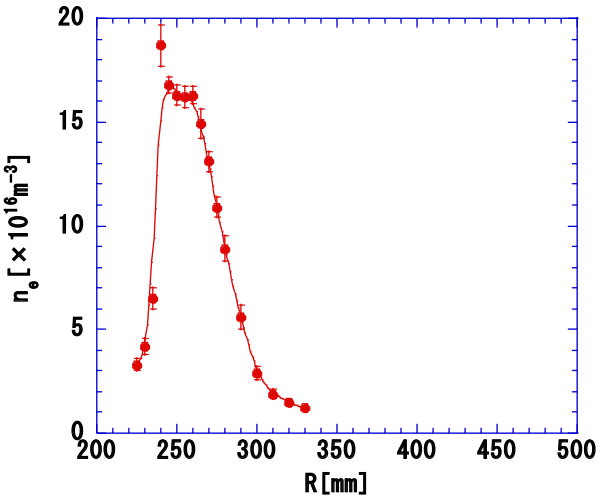

Figure 5.15: Electron Density Profile with F-Coil Levitated

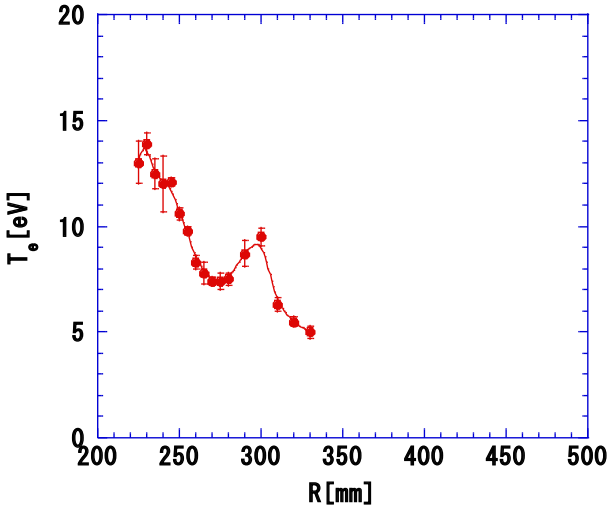

Figure 5.16: Electron Temperature Profile with F-Coil Levitated

electron density is approximately $2.0 \times 10^{17}\mathrm{m}^{-3}$ which corresponds to more than 2.5 times of 2.45GHz O-Mode cutoff density ($7.4 \times 10^{16}\mathrm{m}^{-3}$).

Figures 5.17 and 5.18 show the waveforms of decay of electron density with F-Coil supported and levitated respectively. Measurement was carried out by microwave interferometer. When the F-Coil is supported, electron density decays with output of microwave or faster. On the other hand, when the F-Coil is levitated, electron density decays with two time constants. One of these is comparable with time constant of microwave output and the other is approximately 300ms. On the other hand, longer time constant of microwave is approximately 200ms. Estimating magnetic field strength $B \sim 0.05T$, electron temperature $T_e \sim$ 10eV and characteristic system size $L \sim$ 300mm which corresponds to the distance between outer diameter of F-Coil and vacuum vessel, Bohm diffusion time $\tau_B = \dfrac{L^2}{D_B} = \dfrac{16BL^2}{T_e}$ ~7.2ms where T_e is in eV. When the F-Coil levitated, particle confinement time is sufficiently longer than Bohm diffusion time.

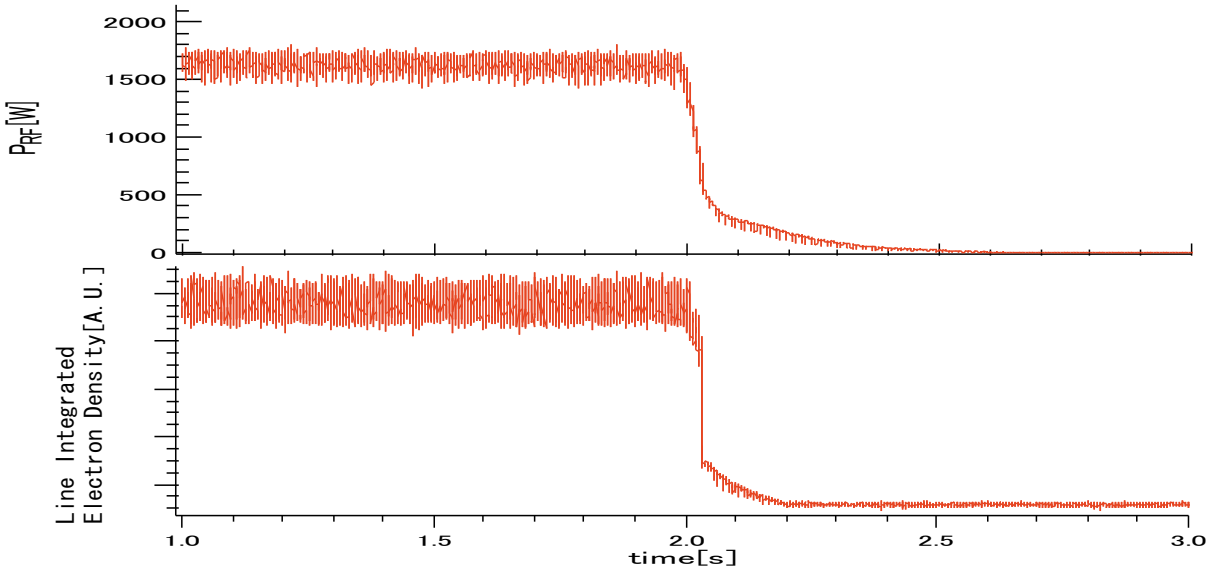

Figure 5.17: Decay of Electron Density with F-Coil Supported

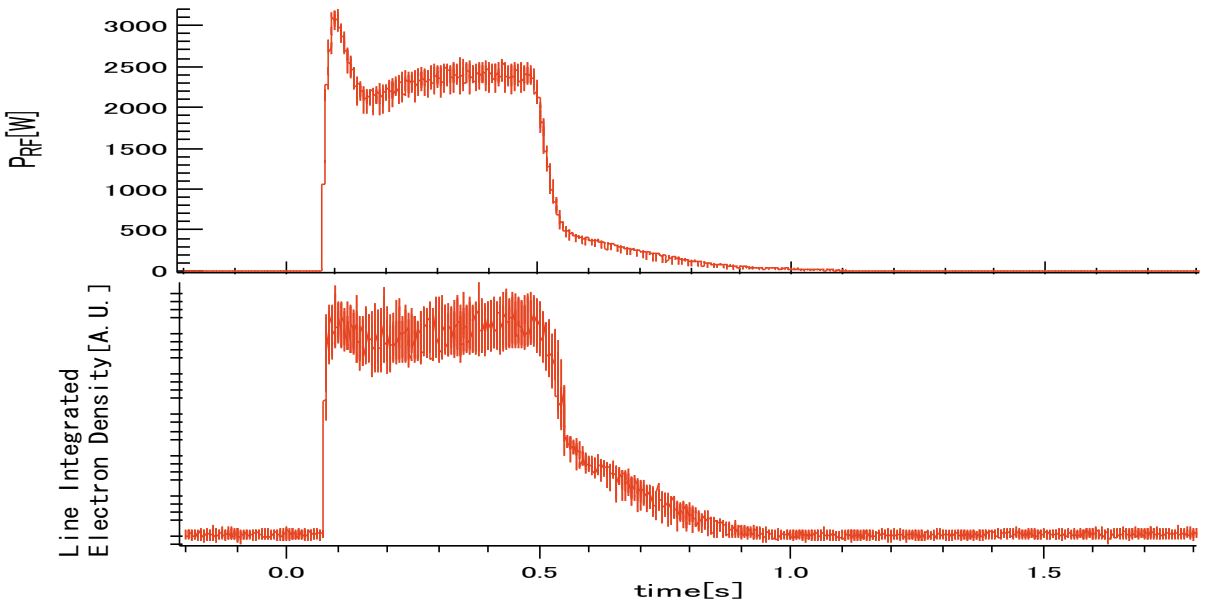

Figure 5.18: Decay of Electron Density with F-Coil Levitated

5.2 Calculated Refractive Indices of Cold Wave and EBW

To investigate excitation, propagation and absorption, refractive indices of cold wave and EBW are calculated. Calculation was carried out along the extension line of the trajectory of incident wave. And equalities of density and temperature on the magnetic surface are assumed. Magnetic field strength in the calculation is on the trajectory, on the

other hand results are shown with respect to major radius R on the midplane to compare with electron density and temperature profiles. A position on the trajectory is translated into R. These are on the same magnetic flux surface.

Trajectory of incident electromagnetic wave is shown schematically in Fig.5.19. Figure 5.20 shows relationship between the coordinates on the trajectory, magnetic field strength there and major radius R on the midplane. And Figs.5.21, 5.22 and 5.23 show refractive indices of X-Wave, EBW and EBW at the vicinity of UHR when L-Coil current is 13.6kA and 2.8kW injection.

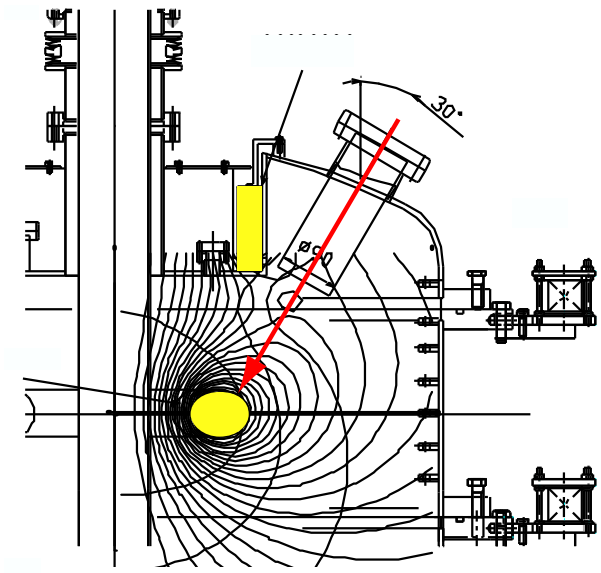

Figure 5.19: Schematic Drawing of Incident Wave Trajectory

Since, as shown in Fig.5.5, electron density does not exceed the cutoff density of O-Wave ($7.4 \times 10^{16}\mathrm{m}^{-3}$), refractive index of O-Wave is always real number. Similarly, L-Cutoff does not appear because of low density. The location of LMET is near $R = 270 \sim 280$mm which almost coincides with 3rd harmonic ECR. Although we can distinguish between the location of 2nd and 3rd harmonic ECR, it is hard to distinguish 3rd and 4th harmonic ECR location in the accuracy of probe measurement, i.e. measurement was carried out every 10mm to investigate the whole of electron density and electron temperature before decaying F-Coil current seriously. It is the fact that electron temperature at the 3rd harmonic ECR is higher than that of at 2nd harmonic ECR.

However, UHR exists between 2nd and 3rd harmonic ECR in this calculation. In this case EBW propagates first for 3rd harmonic ECR and returns for 2nd harmonic ECR and be absorbed there. If the measurement of electron density and magnetic field strength

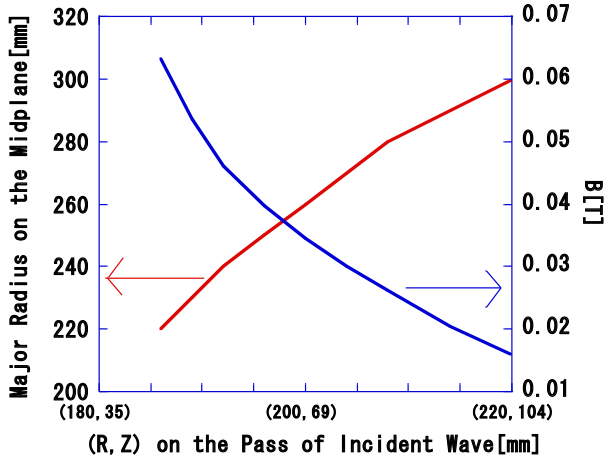

Figure 5.20: Major Radius on the Midplane, Coordinates on Trajectory and B Profile

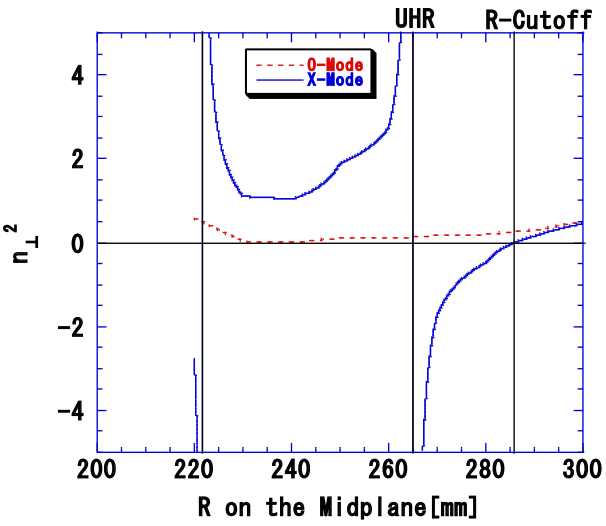

Figure 5.21: Refractive Indices of Cold Waves

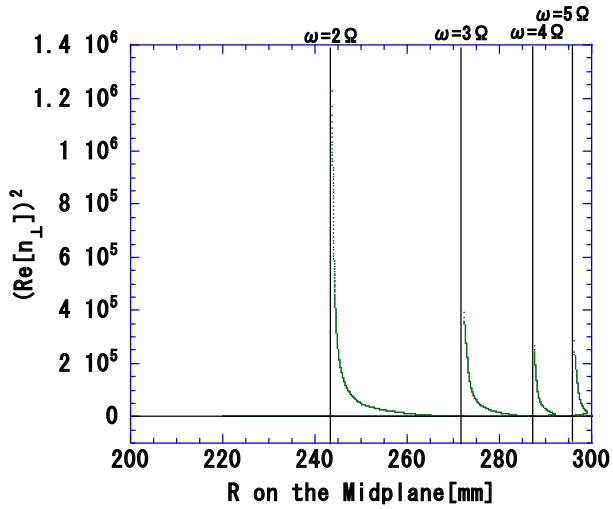

Figure 5.22: Refractive Index of EBW

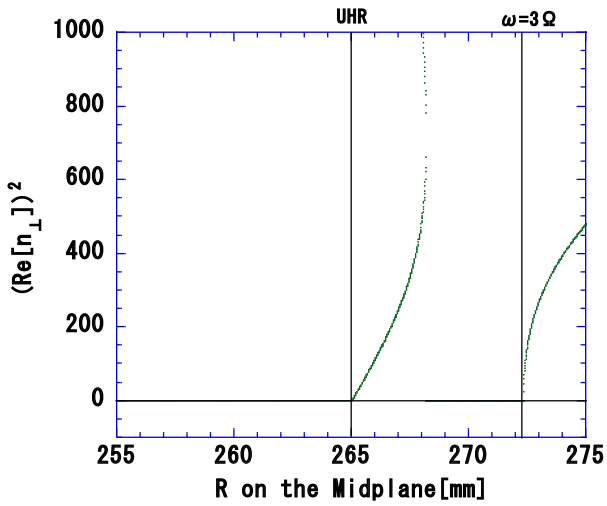

Figure 5.23: Refractive Index of EBW at the Vicinity of UHR

and the assumptions of calculation are correct, this result, i.e. resonance at 2nd harmonic ECR, conflict with experimental result. The effect of error of measurement must be considered.

Assuming that probe measurement has error ±10%, the location of UHR seriously move. Figures 5.24 and 5.25 show the refractive index of X-Wave at the case of artificially increasing and decreasing 10% of electron density respectively which is measured by triple probe uniformly. As shown in Fig.5.21, the location of UHR by using measured electron density is R = 265mm (magnetic flux surface is characterized as major radius on the

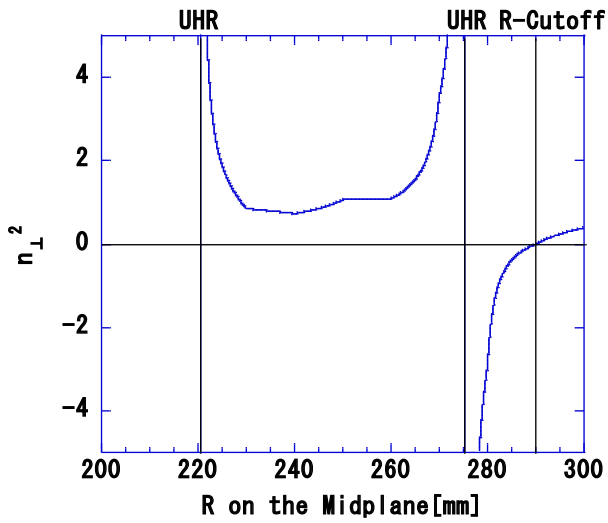

Figure 5.24: Refractive index of X-Wave for artificially increasing electron density

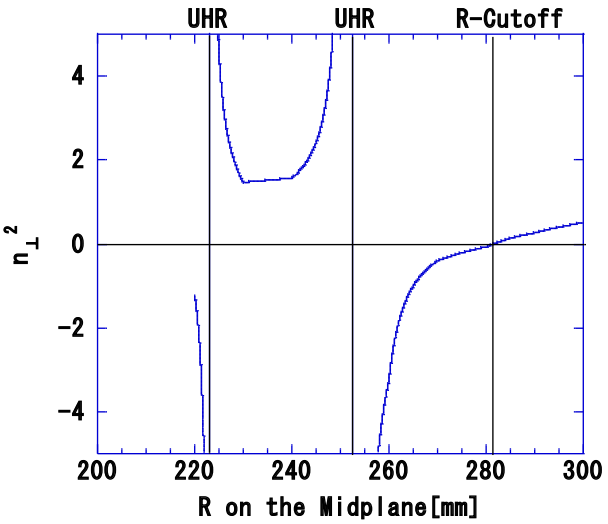

Figure 5.25: Refractive index of X-Wave for artificially decreasing electron density

midplane). If electron density is approximately 10% underestimated, UHR location moves to R =275mm. By contraries, if electron density is approximately 10% overestimated, UHR location moves to R =252mm. Thus the location of UHR drastically changes with error of probe electron density measurement. On the device which has steep magnetic field or density gradient like Mini-RT it is hard to predict the location where EBW is absorbed. From here we focus discussion whether the LMET exists or not. Comparison between location of LMET and that of nth harmonic ECR is continued.

LMETs also exist for the I_L=6.8kA, 2.8kW injection case and I_L=13.6kA, 1.8kW injection case. Figures 5.26 and 5.27 show the refractive index of EBW for the cases of I_L=6.8kA, 2.8kW injection and I_L=13.6kA, 1.8kW injection respectively. In the former case, LMET is at $R = 320 \sim 330$mm while 4th harmonic ECR is at $R = 310$mm. In the latter case, LMET is at $R \sim 300$mm while 3rd harmonic ECR is at $R = 304$mm.

Each of three cases, peak electron density is approximately cutoff density of O-Wave. Thus UHR exists in the range of probe measurement. And the locations of LMET and nth harmonic ECR almost coincident.

In remaining cases, UHR do not exist in the probe measurement range. This means UHR exists inner side of 2nd harmonic ECR. It is impossible to distinguish EBW absorption and fundamental ECH by the electron density and temperature measurements using probe. In these cases, no LMET appears.

Since LMET appears when the electron density is comparable to O-Mode cutoff density

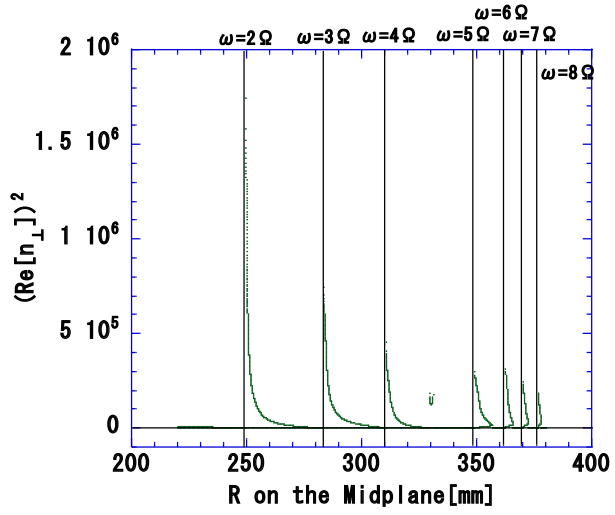

Figure 5.26: Refractive index of EBW for I_L=6.8kA P_{in} =2.8kW

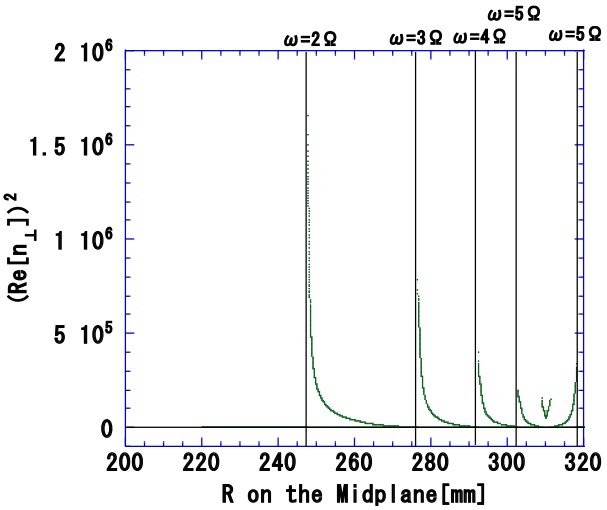

Figure 5.27: Refractive index of EBW for I_L=13.6kA P_{in} =1.8kW

and it exists at ECR, heating by EBW is suggested.

5.3 Conversion Efficiency to EBW

For several cases, conversion efficiency from X-wave to EBW is calculated based on K.G. Budden's theory, i.e. Eq.(3.105). Table 5.4 shows the experimental condition, electron density, magnetic field strength, these gradient lengths at UHR and calculated mode conversion efficiency C. The reason why K.G. Budden's theory was used is that there is no

Table 5.4: Conversion Efficiency

Experimental Condition	$n_e\|_{UHR}$ [m^{-3}]	$B\|_{UHR}$ [T]	$L_n\|_{UHR}$ [cm]	$L_B\|_{UHR}$ [cm]	C [%]
P_{in}=0.8kW, I_L=0, 6.8, 13.6kA	—	—	—	—	—
P_{in}=1.8kW, I_L=0A	—	—	—	—	—
P_{in}=2.8kW, I_L=0A	6.7×10^{16}	0.029	—	0.069	1.5
P_{in}=1.8kW, I_L=6.8kA	4.5×10^{16}	0.055	4.5	4.6	20
P_{in}=2.8kW, I_L=6.8kA	7.0×10^{16}	0.021	6.5	3.0	24.8
P_{in}=1.8kW, I_L=13.6kA	7.2×10^{16}	0.016	3.0	7.4	20
P_{in}=2.8kW, I_L=13.6kA	6.5×10^{16}	0.032	3.9	4.3	24.4

L-Cutoff at these experimental condition. A.K. Ram's theory considers reflected X-Wave at L-Cutoff. So mode conversion efficiency is less than 25%. In the case of P_{in}=2.8kW

and I_L=0A, electron density is flat at UHR. Thus we use $L_n \gg L_B$. Gradient lengths were calculated on the trajectory of incident X-Wave. For 0.8kW injection case, UHR did not appear in measurement range of triple probe. High mode conversion efficiency corresponds to existing of LMET. However for the case of P_{in}=1.8kW and I_L=6.8kA, location of UHR is near the inner edge of measurement region. We cannot discuss about existing of LMET.

Although calculation of conversion efficiency also suggested the possibility of heating by EBW, note that K.G. Budden's theory is slab model. Since Mini-RT is a torus device, UHR layer closes in device. Thus if reflection at L-Cutoff does not occur, X-Wave may access UHR from high field side. Or reflection at F-Coil may lead similar phenomena.

Chapter 6

Future Development

In this chapter future plans related to this study is mentioned.

6.1 Direct Measurement of Conversion Efficiency

There are some interesting method to measure the conversion efficiency from electromagnetic wave to EBW [3][25]. In these methods radiation of X-wave generated by inverse process of FX-SX-B conversion, i.e. B-SX-FX conversion. Black body temperature corresponding the intensity of generated X-wave which is defined as radiation temperature is measured and the ratio of radiation temperature and electron temperature measured by some method, e.g. Thomson scattering, gives conversion efficiency. On the other hand, in this study conversion efficiency were inferred from the results of profile measurements and the theory of mode conversion advanced by A.K. Ram[23].

Direct measurement of conversion efficiency is interesting and very important to investigate the mechanism of generation and heating of overdense plasma. Radiometry or reflectometry of X-wave which has characteristic frequency needs waveguide whose size corresponds to wavelength of X-wave. We must consider the consistency of measurement by allowing for the scale length of density gradient is less than 10cm.

6.2 Energy Measurement of Hot Electron

Detect of high energy electron temperature may be required. As mentioned in Chapter3, absorption of the wave is investigated by knowing the property of dielectric tensor. Ab-

sorption cannot be treated without considering finite Larmor radius effect. If the distribution function of electron velocity is extremely deviated from Maxwellian, dielectric tensor is not written as Eq.(3.70). Absorption to high energy electron is quite large because of its large Larmor radius. And the measurement of high energy electron density and temperature also gives us the modification of electron pressure which is very important parameter when we consider the equilibrium of plasma.

It is well known that high energy electrons are generated by ECH[26]-[28]. Temperature limit in ECH hot electron plasmas are investigated by N.A. Uckan[29] and scaling law is discovered.

$$\rho_e L = 0.05 \sim 0.06 \tag{6.1}$$

Here ρ_e and L denote the relativistic electron Larmor radius and magnetic field scale length (magnetic field radius of curvature) respectively.

Applying this scalling to fundamental ECH of Mini-RT, magnetic field scale length is L ∼5cm. Thus ρ_e ∼2.5mm is obtained. This corresponds to 4-5keV hot electron Larmor radius.

Pulse height analysis using Si(Li) semiconductor detector is planned on Mini-RT. Sensitive region of this detector is 2-30keV.

6.3 Radial Electric Field generation

To drive plasma flow in toroidal direction, radial electric field is needed to generate. An idea to generate radial electric field was proposed by using the orbit loss of hot electron. Numerical analysis of orbit loss was carried out by single particle motion model. However it is necessary to verify the consistency of this model, e.g. from the view point of ambipolar diffusion.

Chapter 7

Summary

Electron cyclotron heating experiments were carried out on internal coil device Mini-RT which has high temperature superconducting floating coil (F-Coil). On the experiments with F-Coil levitated, overdense plasma was generated.

To investigate the mechanism of generation and heating of overdense plasma, consideration of mode conversion from electromagnetic wave to electron Bernstein wave (EBW). EBW has no cutoff density and resonances at any harmonic ECR. Since EBW is electrostatic wave, thus we cannot launch it from outside of vacuum vessel. Therefore some method of mode conversion is needed.

On Mini-RT X-Wave injection from low field side is considered a reasonable method because of weak magnetic field and steep density gradient. To investigate the possibility of heating by EBW, following experiments with F-Coil supported were carried out.

- Changing the plasma confinement region by applying levitation coil current.
- Changing the microwave incident power to move the location of upper hybrid resonance.

Measurements of electron density and electron temperature were carried out by mainly triple probe. The results of electron density measurement by triple probe was consistent with that of 75GHz microwave interferometer.

The results of experiments were summarized as follows.

- Local maximum of electron temperature (LMET) appeared when microwave incident power was sufficiently strong and density gradient was steep.

- However electron density exceeded 2.45GHz O-Wave cutoff density when F-Coil was levitated.

- When F-Coil was levitated, decay of electron density was notably longer than that with F-Coil was supported.

And using the dispersion relations of cold waves and EBW, excitation, propagation and absorption of EBW is analyzed. Analysis was based on electron density and temperature profile measured by triple probe and assumption of uniformity of electron density and electron temperature on magnetic flux. The results of analysis were summarized as follows.

- The location of LMET almost coincides with the location of nth harmonic ECR.

- Since the location of UHR drastically changes by measurement error, inferred location of EBW absorption did not coincide with the results of experiments.

It is the fact that LMET exists at characteristic number of harmonic ECR. The experimental results give suggestions of heating by EBW. However overdense plasma could only be generated at the experiments with F-Coil levitated. In the range of microwave incident power $\sim$3kW, energy confinement time is dominant whether overdense plasma is generated.

Acknowledgements

The author appreciates the members of Ogawa laboratory, Yoshida-Furukawa laboratory and many of relevant parties.

First of all, the author is much grateful to Professor Yuichi Ogawa for his scientific recommendation and educational instruction. He took the base of this study to the author. The author also acknowledge Professor Zensho Yoshida and Associated Professor Masaru Furukawa for their scientific indication.

The author also appreciates for the member of Mini-RT experimental group. Mr.Junji Morikawa always teaches experimental techniques kindly. This study could not be carried out without his advice. Mr.Takuya Goto supported the author and present experimental group kindly. Experimental setup with him made the author to understand about Mini-RT device. Mr.Hajime Kato and Mr.Daisuke Sakata assisted experimental setup and measurements. Especially, assembling of Mini-RT which is moved from Hongo Campus to Kashiwa Campus could be pulled off due to their collaboration. And many private companies (Vega Technology Co., Sanyu Engineering Co., Cryovac Co., IBM Co. and Sanei Giken Co.) assisted to experimental setup.

The author appreciates for Proto-RT experiment and RT-1 construction group, Mr.Sho Watanabe and Mr.Yoshihisa Yano. And the author appreciates for theoretical group of the laboratory, Mr.Makoto Hirota, Mr.Dan Hori, Mr.Jun-ya Shiraishi and Mr.Shuhei Numazawa. The author also appreciates for Mr.Toru Terai and Mr.Kazumasa Shintoku.

The author also appreciates Associated Professor, in Kyoto institute of Technology, Haruhiko Himura. He gives the author many advice about basic of experiments. And the author appreciates Mr.Tomonari Kurihara and Mr.Atsushi Wada.

The author is grateful to Ms.Sunami Kojima and Ms.Nami Tonegawa for their support in daily life.

Last of all, the author appreciates for his family and their support since he was born.

Appendix A

Details about Mini-RT

A.1 High Temperature Superconducting Coil

For the material of F-Coil wire rod on Mini-RT, Bi-2223 tape was adopted. The reason why this material was adopted was as follows.

- Low temperature superconductor (LTS) needs cooling by liquid He. On the other hand, high temperature superconductor (HTS) can be used with a temperature several 10K.
- Thermal likelihood of HTS is larger than that of LTS.
- Workability of Bi-2223 is better than that of YBCO.

However there are some demerits of HTS. Current density of HTS is lower than that of LTS. And HTS is more expensive than LTS.

Since HTS coil does not need liquid He, direct cooling by He gas was adopted for cooling HTS coil on Mini-RT. This method enables to fast cooling compared to cooling by thermal conduction. It is hard for thermal conduction method to balance cooling and thermal insulation. Direct cooling method needs detachable transfer tube and seal construction to avoid leak He gas into vacuum vessel from transfer tube inlet.

Direct charging method by using persistent current switch (PCS) was adopted on Mini-RT. Induction charging needs more than 100kA induction coil and large power supply of induction coil to charge F-Coil 50kA while direct charging method needs less than 2kW power supply. Direct charging method needs detachable current lead.

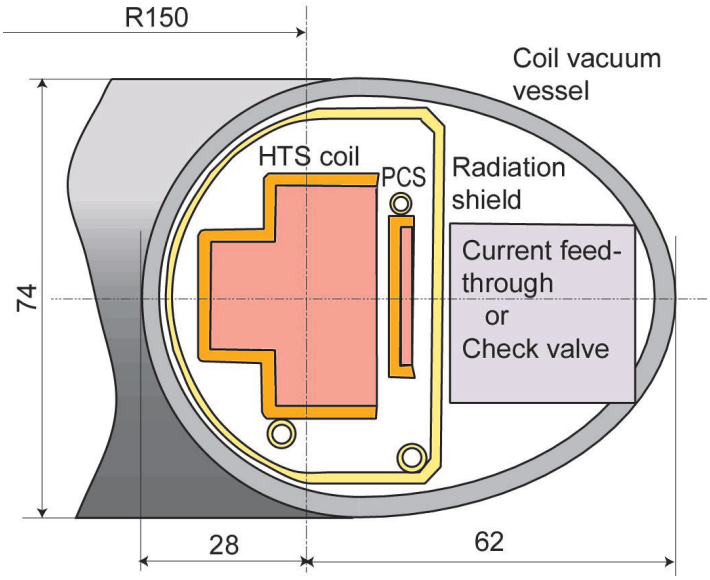

Figure A.1: Cross Section of F-Coil

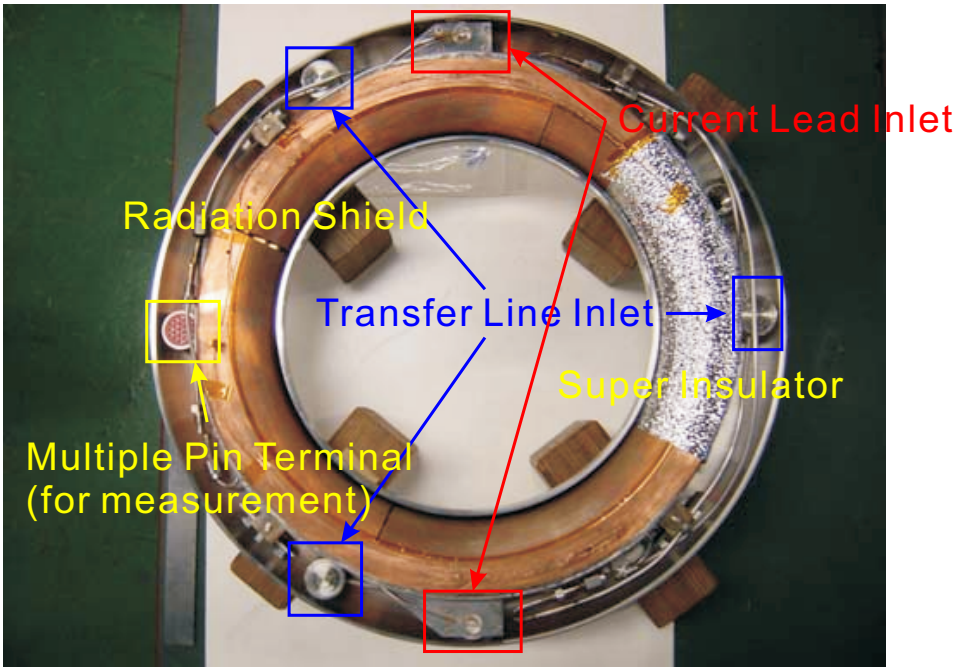

Figure A.2: Top View of F-Coil

Figures A.1 and A.2 show the cross section and top view of F-Coil respectively. Although PCS is made of HTS, however, HTS coil means main HTS coil (not PCS) in this paper. HTS coil and PCS are covered with Copper radiation shield. HTS coil is supported by five folded tube to decrease the thermal load into the radiation shield by keeping distance between the F-Coil shell and the radiation shield. Structure and photograph of five folded tube is shown in Fig.A.3.

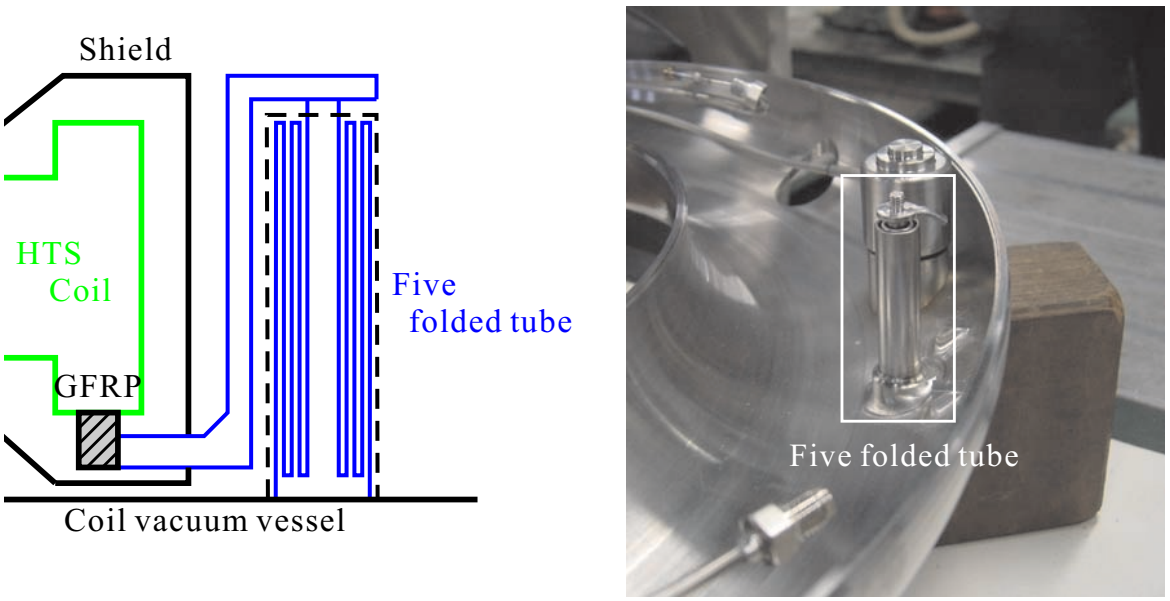

Figure A.3: Structure and Photograph of Five Folded Tube

A.2 Cooling System on Mini-RT

Cooling system is shown in Fig.A.4. Two GM refrigerators are used for cooling He gas. Cooled He gas is compressed to 1MPa and fed to F-Coil through transfer tube. Since it is necessary to control temperatures of HTS coil and PCS independently, there are two recovery transfer tubes.

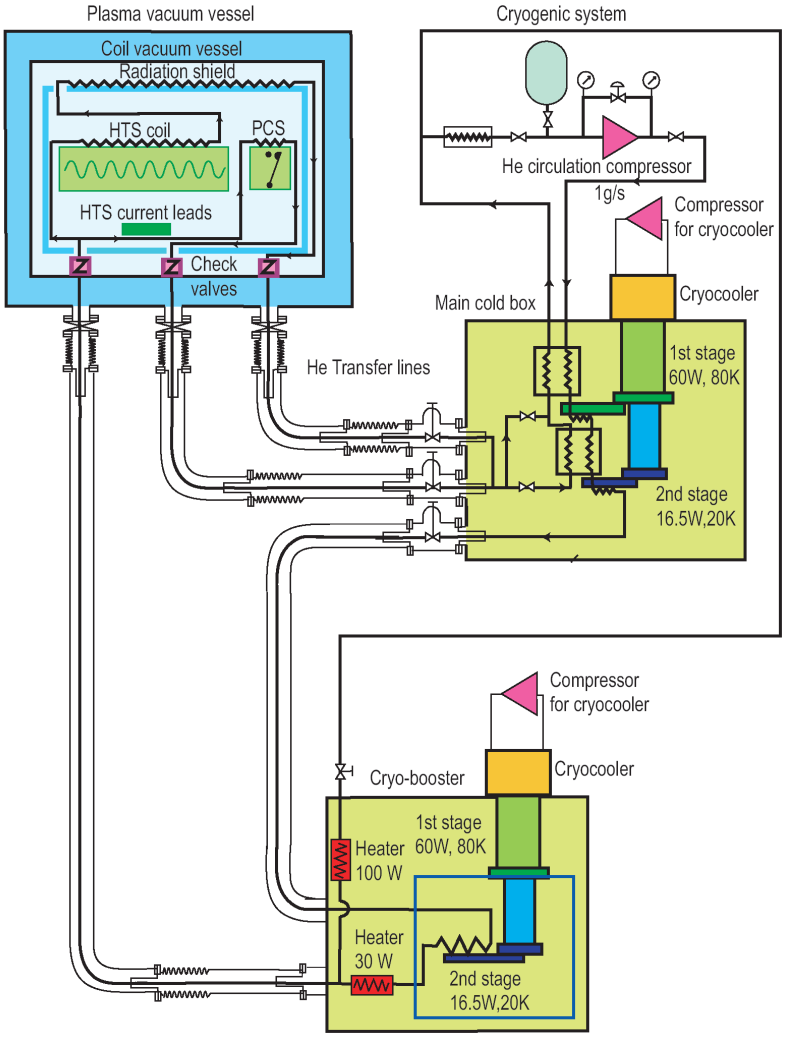

Figure A.4: Cooling System on Mini-RT

The head of transfer tube is shown in Fig.A.5. Projection from the center of transfer tube head opens check valve. The diameter of check valve is 30mm. Six holes are the paths of He gas flow. And right outside of it is Kel-F packing which hardly shrink to avoid leak He gas into vacuum vessel. Fastening the screw at the edge of transfer tube head applies pressure at the seal section and these screws fix transfer tubes mechanically.

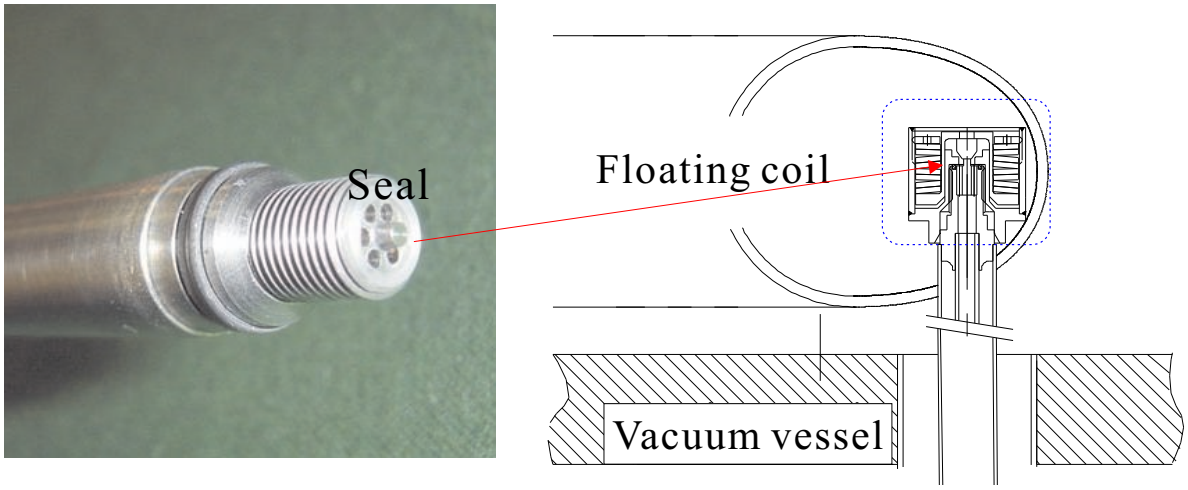

Figure A.5: Detachable Transfer Tube;The Head of Transfer Tube (left), Cross Section of Check Valve (right)

A.3 Charging System on Mini-RT

The schematic view of the charging system is shown in Fig.A.6. Charging sequence is

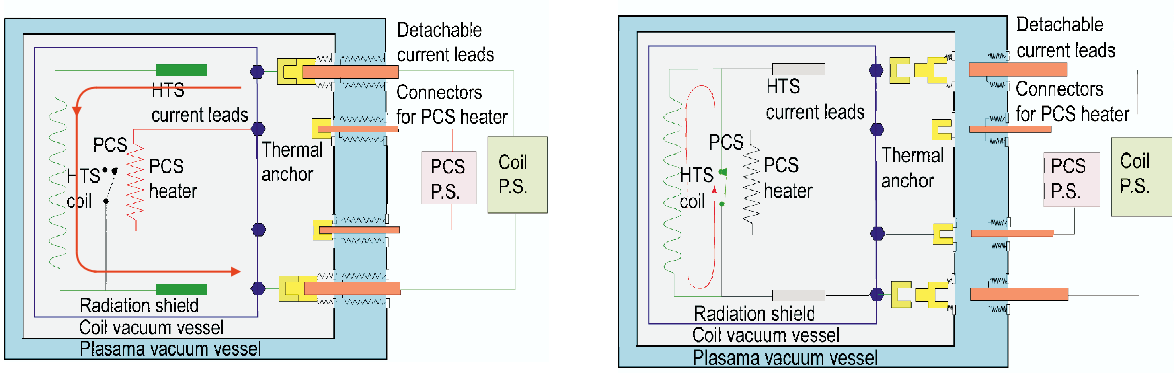

Figure A.6: Schematic View of Charging System

as follows.

1. Connect the current leads for applying current to HTS coil and PCS heater.
2. Heat PCS to ∼130K by using PCS heater (0.8A, 140V). Then PCS is not superconducting state.
3. Apply current to HTS coil.
4. Cool down PCS. Then PCS is also superconducting state.

5. Decrease applying current. Then magnetic flux conservation leads to switching current from HTS coil power supply to PCS.

Figure A.7 shows the photograph of detachable current lead head. Contact resistance between current lead and feed-through is less than 0.5mΩ. To decrease heat load, current lead is cooled by using liquid N_2.

Figure A.7: Photograph of Head of Detachable Current Lead

A.4 F-Coil Levitation System

Pull-up method was adopted for levitation of F-Coil on Mini-RT. Figure A.8 shows the measurement method of F-Coil position. There are three laser position sensor. Vertical position and tilting can be measured by present system. Planned two sensor which measure F-Coil position from horizontal direction will measure the sliding of F-Coil. Figure A.9 shows the top of Mini-RT vacuum vessel where components of levitation is collected.

Tilting stability was discussed and result is shown in Fig.A.10. F-Coil does not tilt by magnetic field of itself. Thus tilting is determined only the geometry of magnetic field created by L-Coil. The ratio of the radii of L-Coil and F-Coil determines the geometry at the surface of F-Coil. In Fig.A.10, L-Coil radius and coordinates are normalized by F-Coil radius. On Mini-RT, L-Coil is near the marginal region.

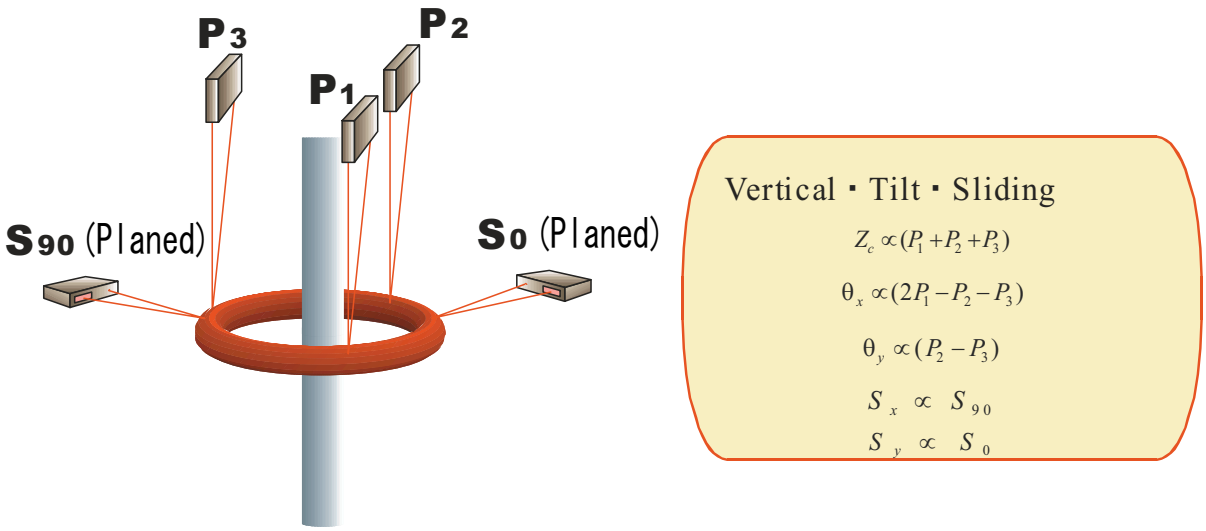

Figure A.8: Measurement Method of F-Coil Position

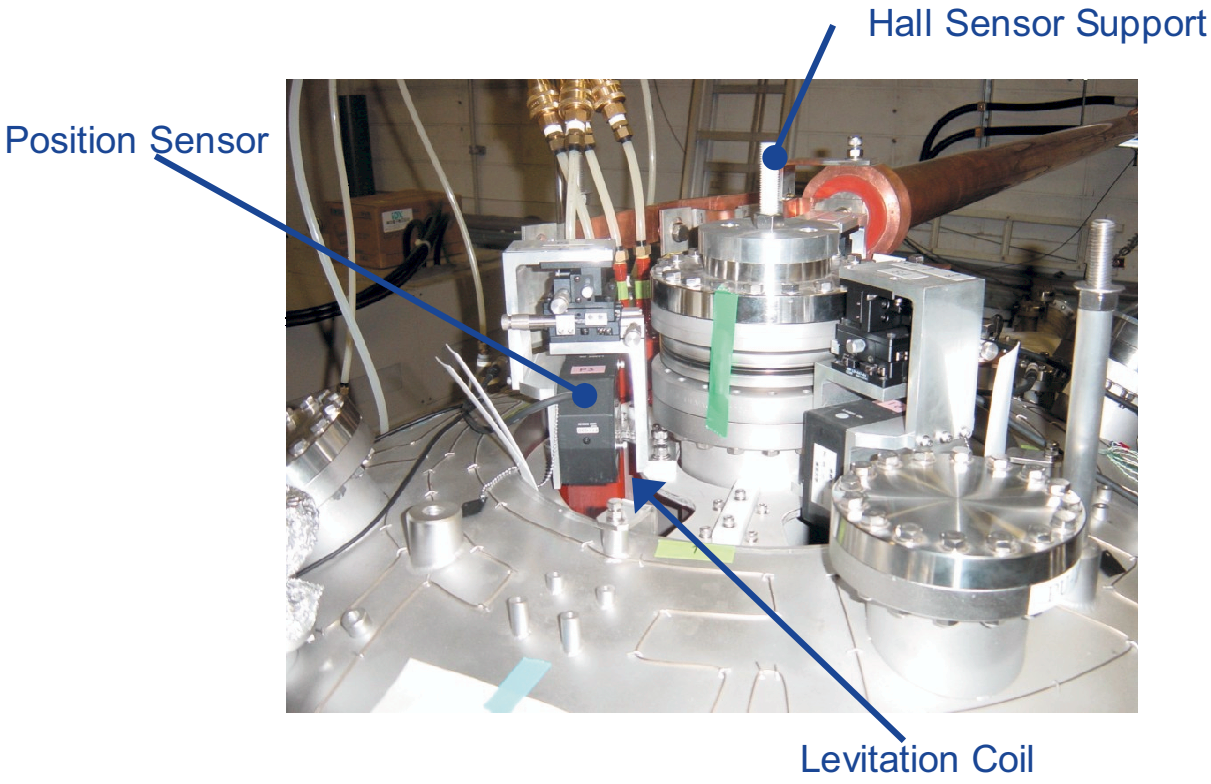

Figure A.9: Photograph of Top of Mini-RT Vacuum Vessel

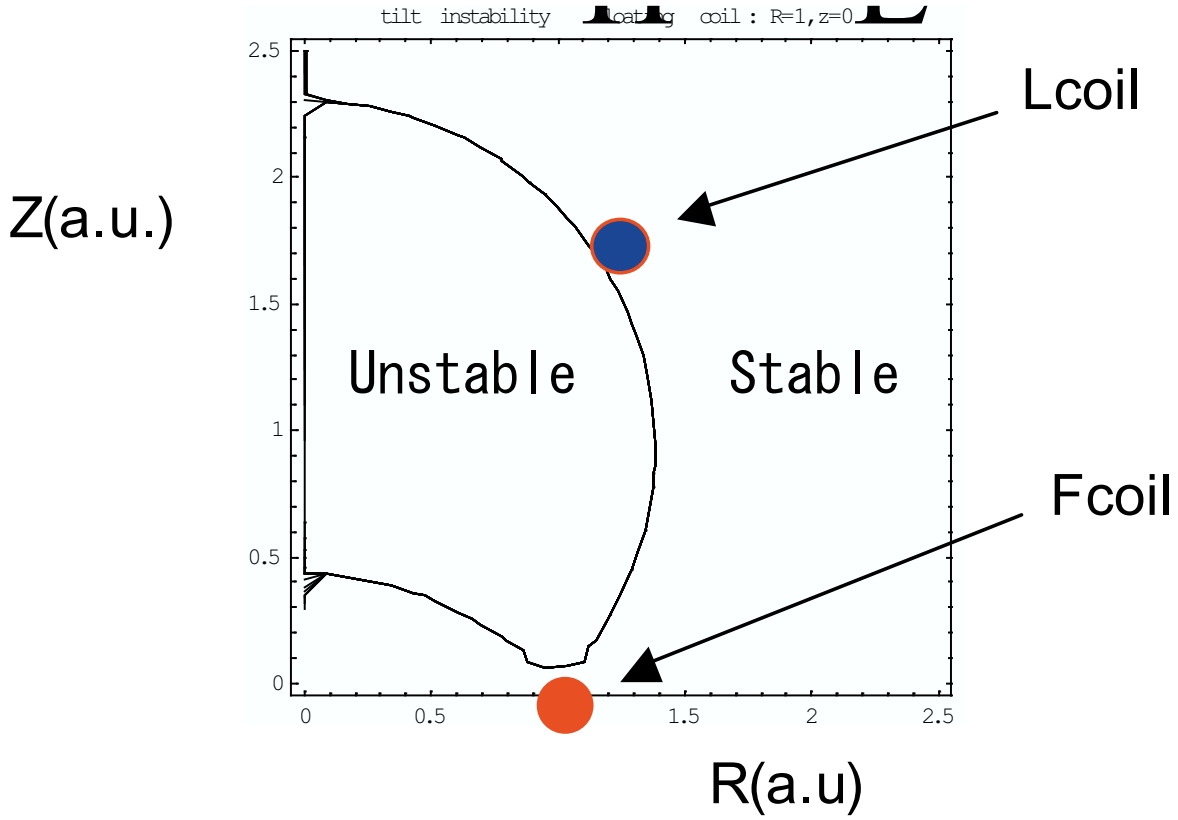

Figure A.10: Tilting Stability

Bibliography

[1] O. Mitarai, *et al.*, "Plasma Current Start-up by ECW and Vertical Field in the TST-2 Spherical Tokamak", J. Plasma Fusion Res. **80** 549 (2004)

[2] I.B. Bernstein, "Waves in a Plasma in a Magnetic Field", Phys. Rev. **109** 10 (1958)

[3] G. Taylor, *et al.*, "Enhanced conversion of thermal electron Bernstein waves to the extraordinary electromagnetic mode on the National Spherical Torus Experiment", Phys. Plasmas **10** 1395 (2003)

[4] H.P. Laqua, *et al.*, "Resonant and Nonresonant Electron Cyclotron Heating at Densities above the Plasma Cutoff by O-X-B Mode Conversion at the W7-AS Stellarator", Phys. Rev. Lett. **78** 3467 (1997)

[5] T. Ohkawa *et al.*, "STABLE PLASMA CONFINEMENT BY MULTIPOLE FIELDS", Phys. Lev. Lett. **7** 41 (1961)

[6] S.A. Colgate *et al.*, "Stabilization of Pinch Discharge", Phys. Fluids **3** 982 (1960)

[7] S. Yoshikawa *et al.*, "Axisymmetric Minimum Average B Configuration of a Triply Connected System", Phys. Fluids **9** 2295 (1966)

[8] S. Yoshikawa, "*Plasma · Fusion*" chapter 31 (in Japanese), Kyoritu Syuppan (1979)

[9] For example, S.M. Krimigis *et al.*, "Hot Plasma Environment at Jupiter: Voyager 2 Results", Science **206** 977 (1979)

[10] A. Hasegawa *et al.*, "A D-^{3}He FUSION REACTOR BASED ON A DIPOLE MAGNETIC FIELD", Nucl. Fusion **30** 2405 (1990)

[11] S.M. Mahajan *et al.*, "Double Curl Beltrami Flow: Diamagnetic Structures", Phys. Rev. Lett. **81** 4863 (1998)

[12] Z. Yoshida *et al.*, "Variational Principles and Self-Organization in Two-Fluid Plasmas", Phys. Rev. Lett. **88** 095001 (2002)

[13] N. Yanagi *et al.*, "Experiments of the HTS Floating Coil System in the Mini-RT Project", IEEE Trans. Appl. Supercond. **14**(2) 1539 (2004)

[14] Y. Ogawa *et al.*, "Construction and Operation of an Internal Coil Device with a High Temperature Superconductor", J. Plasma Fusion Res. **79** 643 (2003)

[15] Stability of levitation for more general case was investigated. J. File *et al.*, "Stabilized, Levitated Superconducting Rings", J. Apl. Phys. **39** 2623 (1968)

[16] J. Morikawa *et al.*, "Levitation Experiment Using a High-Temperature Superconducting Coil for a Plasma Confinement Device", Jpn. J. Apl. Phys. **40** L1029 (2001)

[17] T.H. Stix, "Waves in Plasmas" chapter 1, American Institute of Physics (1992)

[18] B.D. Fried *et al.*, "The Plasma Dispersion Function", Academic Press, New York (1961)

[19] F.W. Crawford *et al.*, "On the Interpretation of Ionospheric Resonances Stimulated by Alouette 1", J. Geophys. Res., **72**, 57 (1967)

[20] K. Miyamoto, "Plasma Physics and Controlled Nuclear Fusion" chapter 10 (in Japanese), University of Tokyo Press (2004)

[21] K.G. Budden, "The Propagation of Radiofrequency Waves" chapter 19, Cambridge University Press (1985)

[22] M. Abramowitz, *et al.*, "Handbook of Mathematical Functions", Dover (1970)

[23] A.K. Ram *et al.*, "Excitation, propagation and damping of electron Bernstein waves in tokamaks", Phys. Plasmas **7** 4084 (2000)

[24] A.K. Ram *et al.*, "Mode conversion of fast Alfvén waves at the ion-ion hybrid resonance", Phys. Plasmas **3** 1976 (1996)

[25] S. Shiraiwa *et al.*, "Electron Bernstein wave emmision diagnostic assisted by reflectmetry on TST-2 spherical tokamak", Rev. Sci. Instrum. **74** 1453 (2003)

[26] H. Ikegami *et al.*, "SHELL STRUCTURE OF A HOT-ELECTRON PLASMA", Phys. Rev. Lett. **19** 778 (1967)

[27] M. Okabayashi *et al.*, "Hot-electron plasma in the levitated spherator", Phys. Fluids **16** 1337 (1973)

[28] H.P. Warren *et al.*, "emission of Chaotic Particle Transport Induced by Drift-Resonant Fluctuations in a Magnetic Dipole Field", Phys. Rev. Lett. **74** 1351 (1995)

[29] N.A. Uckan, "Temperature limit in ECH hot electron plasmas", Phys. Fluids **25** 2381 (1982)

Related Presentation

- E. Yatsuka, T. Goto, J. Morikawa and Y. Ogawa, "ECH Plasma Characteristic of the Internal Coil Device Mini-RT", 8th Meeting of Plasma Study by the Young Scientists, JAERI(JAEA), 16-18 March 2005, 11
- E. Yatsuka, T. Goto, H. Kato, D. Sakata, J. Morikawa, Y. Ogawa, N. Yanagi and T. Mito, "Study on ECH Plasma Experiments for Generation of High Energy Electrons on the Internal Coil Device Mini-RT", JPS Autumn Meeting, Kyoto, 19-22 September 2005, 19aW3
- E. Yatsuka, H. Kato, D. Sakata, T. Goto, J. Morikawa, Y. Ogawa, N. Yanagi, T. Mito, "Plasma Property for ECH Injection Mode on the Internal Coil Device Mini-RT", JSPF Annual Meeting, Tokyo, 29-30 November 1-2 December 2005, 29aC39P